Determination of the $\pi^{\pm}p \rightarrow \pi^{\pm}\pi^{+}n$ cross section near threshold

J. B. Lange,* A. Ambardar, F. Duncan,† A. Feltham, G. Hofman, R. R. Johnson, G. Jones, M. Pavan,‡ K. J. Raywood, and D. Vetterli§
Department of Physics, University of British Columbia, Vancouver, British Columbia, Canada V6T 1Z1

J. T. Brack,‖ D. Ottewell, and G. R. Smith
TRIUMF, 4004 Westbrook Mall, Vancouver, British Columbia, Canada V6T 2A3

M. E. Sevior¶
School of Physics, University of Melbourne, Parkville, Victoria 3052, Australia
(Received 2 July 1999; published 13 January 2000)

The total cross section for the $\pi^{-}p \rightarrow \pi^{-}\pi^{+}n$ reaction has been measured at incident pion kinetic energies of 200, 190, 184, 180, and 176 MeV, and cross sections for the $\pi^{+}p \rightarrow \pi^{+}\pi^{+}n$ reaction were obtained at 200 and 184 MeV. A fit of these cross sections by heavy baryon chiral perturbation theory yields values of 8.5 $\pm 0.6(m_{\pi}^{-3})$ and $2.5 \pm 0.1(m_{\pi}^{-3})$ for the reaction matrix elements $\mathcal{A}_{10}$ and $\mathcal{A}_{32}$, and, for the *s*-wave isospin-0 and isospin-2 π-π scattering lengths, the values $a_0 = 0.23 \pm 0.08(m_{\pi}^{-1})$ and $a_2 = -0.031 \pm 0.008(m_{\pi}^{-1})$, respectively.

PACS number(s): 25.80.Ek, 13.60.Le, 13.75.Gx, 13.85.Hd

I. INTRODUCTION

Though widely successful in particle physics, QCD is notoriously difficult to apply at low energies. However, exploitation of the symmetries of QCD [1] via chiral perturbation theory (ChPT) has enabled such questions as the determination of the strength of the simplest example of the strong interaction, the π-π, to be addressed. These theories are most relevant in the low-energy limit, a region which includes such quantities as the *s*-wave isospin-0 and isospin-2 π-π scattering lengths (a_0 and a_2).

Because of the experimental intractability of a direct determination of the π-π scattering lengths through measurements of free π-π scattering, indirect techniques have been utilized. The reactions that have been most extensively investigated include the $Ke4$ kaon decays ($K^{+} \rightarrow \pi^{+}\pi^{-}e^{+}\nu_e$) which are sensitive to a_0, and pion-induced pion production reactions such as ($\pi p \rightarrow \pi\pi n$) which are sensitive to both a_0 and a_2. The advantage of investigating *K* decay is that the only strongly interacting particles which occur in the final state are the two pions of interest. The best $Ke4$ experiment performed to date is that reported by Rosselet *et al.* [2] who studied the decay $K^{+} \rightarrow \pi^{+}\pi^{-}e^{+}\nu_e$. However, an accurate measurement of a_0 requires good statistics, and as a result of collecting data for four months, the Rosselet *et al.* experiment obtained only 30 000 events, resulting in a 20% uncertainty in their value for $a_0(0.26 \pm 0.05)$.

The $N(\pi,2\pi)N$ reactions are sensitive to π-π scattering because one pion exchange (OPE) is a dominant mechanism. Although additional sizable backgrounds from other processes also contribute, such backgrounds can be understood in terms of heavy baryon chiral perturbation theory (HBChPT) if the measurements are performed close to threshold. Since these $(\pi, 2\pi)$ reactions involve the strong interaction, adequate statistics can be attained over much shorter time periods, of the order of a few days.

In 1978, Kravtsov *et al.* [3] obtained information on the $\pi^{+}p \rightarrow \pi^{+}\pi^{+}n$ reaction from measurements of the charge symmetric reaction extracted from the more complex $\pi^{-}d \rightarrow \pi^{-}\pi^{-}pp$ reaction. These data were obtained for pion beam energies of 230–360 MeV, more than 60 MeV above the reaction threshold. In 1989, Sevior *et al.* [4] determined the energy dependence of the total cross section for the $\pi^{+}p \rightarrow \pi^{+}\pi^{+}n$ reaction in the threshold region, obtaining results consistent with the higher energy data of Kravtsov. Since their cross-sections were measured within 8 MeV of threshold, Sevior *et al.* were able to provide better data for evaluating the $\pi^{+} - \pi^{+}$ isospin-2 scattering length, a_2.

However, before the paper of Sevior *et al.* was published, the OMICRON Collaboration [5] reported the results of an experiment which spanned the pion kinetic energy ranges of both Kravtsov *et al.* and Sevior *et al.*, as illustrated in Fig. 1. The OMICRON results, although generally consistent with the data of Kravtsov *et al.* at energies above 300 MeV, were in disagreement with the results of Sevior *et al.* nearer threshold. In addition to the π^{+} reaction channel, the OMICRON Collaboration also obtained data for the π^{-} channel, $\pi^{-}p \rightarrow \pi^{-}\pi^{+}n$ [5]. As shown in Fig. 2 these results agreed with those obtained earlier by Bjork *et al.* [6].

In 1991, Burkhardt and Lowe [7] carried out an amplitude analysis of all the data available at the time for the five

*Present address: Defense Research Establishment Ottawa, Nepean, Ontario Canada K1A 0Z4.
†Present address: Dept. of Physics, Queen's University, Kingston, Ontario Canada K7L 3N6.
‡Present address: MIT, Cambridge, MA 02139.
§Present address: Inselspital—University of Bern, Division of Medical Radiation Physics, CH-3010 Bern, Switzerland.
‖Present address: Dept. of Physics, University of Colorado at Boulder, Boulder, CO 80309-0390.
¶Electronic address: msevior@physics.unimelb.edu.au

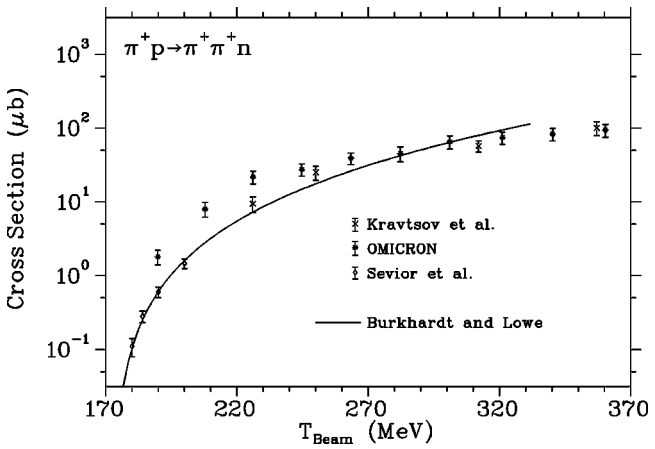

FIG. 1. The world's data set for $\pi^+ p \to \pi^+ \pi^+ n$ prior to 1993. The references for the data are OMICRON [5], Kravtsov *et al.* [3], Sevior *et al.* [4], and Burkhardt and Lowe [7].

channels of the $(\pi p \to \pi\pi n)$ reaction in order to test the overall consistency of the data as well as to provide a check on the model of Olsson and Turner [8] which represented the π-π interaction in terms of the chiral symmetry breaking parameter ξ. This analysis indicated an acceptable degree of consistency between all the published data for energies above 250 MeV. However an acceptable χ^2 for their global fit was only possible if the Kravtsov and Omicron data for the $\pi^+\pi^+$ reactions below 255 MeV were excluded from the fit. A later global analysis by Pocanic *et al.* [9] which included their new $\pi^+\pi^0$ data also excluded the low energy data points of the OMICRON group for the $\pi^+\pi^+$ channel. Unfortunately the new $\pi^+\pi^0$ data included in this fit do not constrain the isospin 2 amplitude at low energies because the data have uncertainties of 40% and greater below 200 MeV.

Although the pion production reactions were traditionally analyzed in terms of the model of Olsson and Turner [8], Olsson and co-workers have recently found [10] that the inclusion of higher-order terms neglected in their earlier work complicated the extraction of π-π scattering lengths from

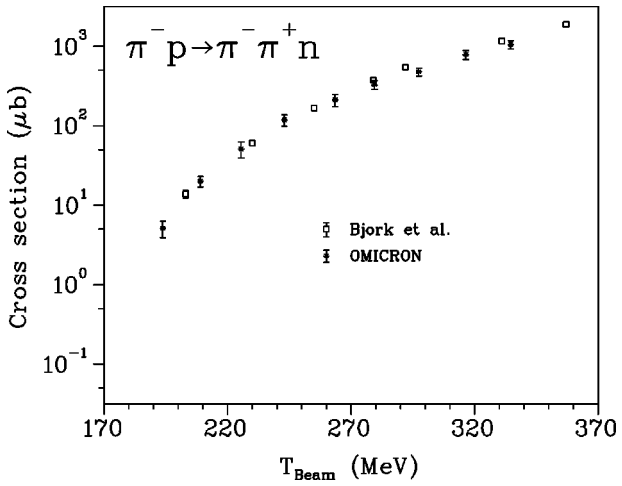

FIG. 2. The world's data set for $\pi^- p \to \pi^- \pi^+ n$ prior to 1993. The references for the data are Bjork *et al.* [6] and OMICRON [5].

threshold pion production data. Moreover, their treatment of the OPE contribution in terms of a parameter, ξ, which is dependent on the strength of the π-π interaction, is inconsistent with ChPT, making any attempt to incorporate higher resonances unreliable. However, Bernard, Kaiser, and Meißner [11] have shown that $(\pi,2\pi)$ reactions can be understood in terms of heavy baryon chiral perturbation theory, a theory which incorporates the effects of higher baryon resonances as well as treating the OPE contribution in a manner consistent with ChPT. Consequently, Bernard *et al.* were able to obtain more reliable relationships between the threshold amplitudes for pion production and the π-π scattering lengths. They emphasized, however, that extraction of the π-π scattering lengths requires the availability of good experimental data near threshold (i.e., below 200 MeV). As the $\pi^- p \to \pi^- \pi^+ n$ reaction involves both the isospin-2 and isospin-0 $\pi\pi$ interaction amplitudes whereas the $\pi^+ p \to \pi^+ \pi^+ n$ reaction involves only isospin-2, determination of both of the isospin amplitudes requires reliable cross-section data for each of the reactions near threshold.

Of major concern was the existence of a discrepancy of more than a factor of two between the $\pi^+ p \to \pi^+ \pi^+ n$ of the OMICRON Collaboration [5] and that of Sevior *et al.* [4], the only two experiments for which data were obtained within 40 MeV of threshold. For the $\pi^- p \to \pi^- \pi^+ n$ reaction on the other hand, a reaction whose cross section is about five times larger than that of the π^+ channel, a consistent body of experimental data existed for the reaction at energies above 200 MeV, with only one data point (provided by the OMICRON Collaboration) for energies below 200 MeV.

The aim of the present experiment was both to provide the necessary cross-section data for the π^- channel at energies below 200 MeV and to resolve the factor of two discrepancy in the π^+ data at these energies. Although most experiments experience more difficulty measuring the π^+ channel cross sections than the π^- because of their small size, the particular technique employed in this experiment is characterized by a cleaner signal for the π^+ channel than for the π^-, a benefit that more than compensates for the smaller cross section values involved.

The experiment was carried out using an improved version of the technique utilized earlier by Sevior *et al.* [4] to measure total cross sections for the π^+ channel. In such an experiment, the final state pions, either π^+-π^+ or π^+-π^-, are sufficiently low in energy that they stop in an ''active'' hydrogenous target (PILOT-U scintillator) [12]. The muon arising from decay of the positive pion is then detected in coincidence with the outgoing neutron. For the π^+ channel, the decay muons from both of the positive pions can be detected, thus leading to enhanced background discrimination. The $\pi^- p \to \pi^- \pi^+ n$ cross sections were measured at incident pion energies of 176, 180, 184, 190, and 200 MeV, while $\pi^+ p \to \pi^+ \pi^+ n$ cross-sections at 184 and 200 MeV were also obtained in order to check the reproducibility of the previous Sevior *et al.* results [4]. The experimental details of the experiment are discussed in Secs. II and III, the π^+ channel results in Sec. IV, the π^- channel results in Sec. V, and a discussion and the conclusions in Secs. VI and VII, respectively.

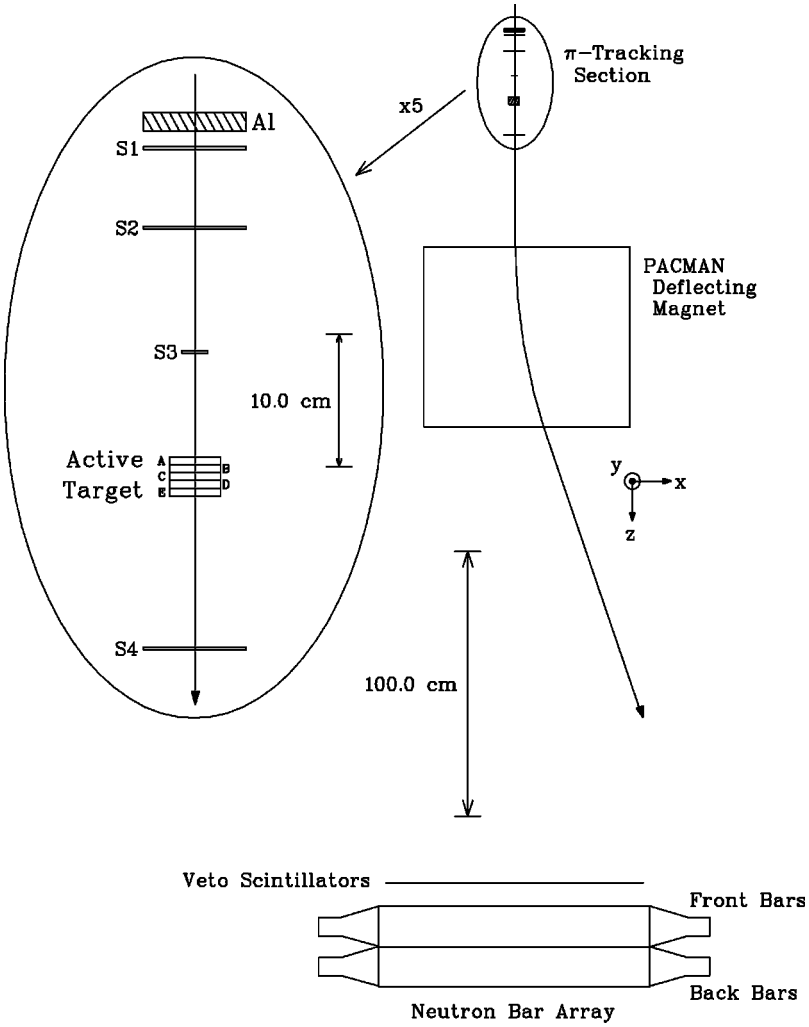

FIG. 3. Layout of the experimental apparatus. The deflection angle shown is for a beam of 200 MeV pions. The placement of Al blocks for the calibration of the individual sections of the active target is also indicated.

II. EXPERIMENTAL CONFIGURATION

The experiment was performed on the M11 beamline at TRIUMF using negative pions of 200, 190, 184, 180, 176, and 172 MeV kinetic energy, and positive pions of 200, 184, and 172 MeV. The 172 MeV data provided background information since this energy is below the threshold for pion production (172.3 MeV).

The apparatus, which was similar to that used by Sevior *et al.* [4], is shown in Fig. 3. The incident pions were tracked by a set of three plastic scintillators ($S1-S3$) of dimensions $80\times80\times2$, $80\times80\times2$, and $20\times20\times2$ mm^3, respectively. The third scintillator was half the transverse size of the target itself while the first two were twice the target size. The reason for selecting large scintillators for $S1$ and $S2$ was to enable detection of particles in the beam halo while the smaller third scintillator, $S3$, restricted the beam interactions to be well within the target dimensions. The pions were discriminated from beam contaminants by a combination of time-of-flight measurement through the $M11$ channel together with detection of the energy loss of the incoming particles in the beam-tracking scintillators.

When a $\pi p \rightarrow \pi\pi n$ reaction occurred within the target, those final state pions contained within the active target were detected together with their daughter muons while the neutrons were detected and identified by an array of fourteen scintillator bars placed 3.0 m downstream of the target. The active target, consisting of five segments of 6 mm thick PILOT-U scintillator ($C_1H_{1.1}$), was followed by a veto scintillator ($S4$) which helped restrict the electronic event definition to those pion interactions occurring in the active target. The photomultipliers associated with all the scintillators comprising the in-beam array and the target elements were connected to analog-to-digital converters (ADCs) and time-to-digital converters (TDCs). For the target scintillators, two ADCs were employed on each, one (short gate) gated for 15 ns and the other (long gate) for 80 ns. In this way, a straightforward determination of the occurrence of a pion decay could be obtained by comparing the pulse heights provided by the short gate and long gate ADCs. In addition to the connection to a TDC and the ADCs, the photomultiplier attached to each target segment was connected to a charge-coupled-device (CCD) transient digitizer [13] which recorded the energy deposited in its target segment in bins of 2 ns width for a total period of 100 ns. The information recorded by the CCDs, along with the ADC signals, enabled unambiguous identification of the muons arising from the decay of the positively charged final state pions. The timing of the experiment was controlled by $S3$, the smallest of the in-beam scintillators.

Background charged particles were cleared from the experimental area by means of a dipole magnet. In addition, an array of veto scintillators preceding the neutron bars was used to discriminate against background signals arising from detection of residual charged particles reaching this part of the system.

While the experimental design was based on the earlier arrangement used by Sevior *et al.* [4], a number of improvements were incorporated into this version. In the current configuration, a further reduction of the neutron background arising from interactions of the incident pions with the carbon in the target was achieved by placing the neutron array 3.0 m downstream of the target rather than 2.6 m as employed by Sevior *et al.*, in order to more strongly exploit the restrictive kinematics of the reaction. For $\pi p \rightarrow \pi\pi n$ reactions, the forward angle cone characterising the outgoing neutrons is bounded by 20°, whereas the neutrons arising from pion absorption in carbon are emitted over 4π. In addition, this experiment employed a second-level trigger based on a comparison of the outputs of the ''short'' and ''long'' gated ADC's, a system which preferentially selected events associated with the decay of a pion in the target. Also, the target phototubes were operated at much lower gain than were those in the original setup of Sevior *et al.* in order to eliminate the aging effect observed in the earlier experiment. Finally, and more importantly, while Sevior *et al.* employed an oscilloscope as a transient digitizer to detect and analyze the secondary pulses in the target, the current configuration utilised fast CCD's attached to each target segment to provide this information.

III. EXPERIMENTAL DETAILS

The cross sections were determined using

$$\sigma = \frac{1}{N_i n_{tgt}} \frac{N_{\text{coinc.}}}{\Pi(\eta_\pi;\eta_n;T_\pi)\Lambda}, \tag{1}$$

where N_i denotes the number of acceptable pions incident on the target, n_{tgt} is the number of hydrogen nuclei per unit area and per 0.1 MeV energy loss of the incident beam, $N_{\text{coinc.}}$ is the experimental yield, Π is the total experimental acceptance, η_π and η_n are the detection efficiencies for the pions and neutrons, respectively, T_π is the kinetic energy of the incident pions, and Λ is the CPU livetime of the data acquisition system. The target thickness is determined in terms of 0.1 MeV steps of the incident pion's energy loss to take account of the rapid variation of the cross section near threshold.

A. Kinematic definition

For a given incident pion energy, the total kinetic energy of the reaction products is well defined. However, a histogram of this total kinetic energy would be broadened due to the energy loss suffered by the pions while traversing the target prior to the reaction of interest (up to 6.6 MeV). This effect could be accounted for in our experiment since the energy loss of the incident pions was also measured, thus enabling the total kinetic energy to be corrected appropriately. Thus, the quantity histogrammed was T_{sum}, where

$$T_{\text{sum}} = T_{\text{scin}} + T_n . \tag{2}$$

T_{scin} is the total energy deposited in the active target: the sum of the energies of the final state pions together with the energy loss of the incident pion prior to the $(\pi, 2\pi)$ reaction, and T_n is the energy of the neutron evaluated from the time-of-flight (TOF) of the neutrons from the active target to the neutron bars. Thus, for an incident pion of kinetic energy, T_{beam}, $T_{\text{sum}} = T_{\text{beam}} - m_\pi - (m_n - m_p)$, a quantity independent of the energy loss suffered by the incident pions while traversing the target. The accumulated counts contained within the appropriate peak of the T_{sum} histograms thus provided the experimental yields.

Since the experiment was performed at less than 30 MeV above threshold, an energy which permitted both product pions to remain within the active target, T_{sum} values ranging from 35 MeV at threshold to 59 MeV (for 200 MeV incident pions) spanned the range encountered in this experiment. After stopping, the positive pions decayed via $\pi^+ \rightarrow \mu^+ \nu_\mu$ whereas the negative pions were captured by the carbon nuclei in the target.

B. Incident beam

As the incident beam did not consist solely of pions (the π^+ beam was contaminated with muons, positrons and protons, whereas the π^- beam also contained muons and electrons), the pion fraction of the beam had to be determined for each of the runs. The protons were discriminated by pulse height cuts placed on the in-beam scintillators, $S1$, $S2$, and $S3$. For the electrons and positrons which are almost 300 times lighter than the pions, times of flight down the M-11 beamline were sufficient to provide ready identification. For the muon contamination, such a technique was not possible, however, since the muon rest mass is so similar to that of a pion. In this case, use was made of previous studies [15] of the beamline which indicated a 1.2% muon contamination at the energy ranges discussed in this paper. The total combined electron and muon contamination amounted to $\sim$3% and, for the π^+, the proton contamination prior to discrimination was $\sim$1%.

The M-11 channel delivered particles to the target area at a typical rate of 1.7 MHz whereas the cyclotron RF frequency was 23.06 MHz [14]. For all beam energies and for both polarities of pion, the incident beam was characterized at the active target by an angular spread of $\pm 1°$ in the horizontal (x-z) plane and $\pm 5°$ in the vertical (y-z) plane, with the focus (approximately 1 cm wide) at the center of the target. The momentum spread of the beam was $\pm 0.1\%$ (± 0.3 MeV at 200 MeV) for π^+ and $\pm 0.5\%$ for π^-. The absolute momentum calibration of the beamline corresponded to an uncertainty of 0.7 MeV at 200 MeV.

C. Event definition

In order to efficiently reject the large background, a two level event triggering system was utilized. By limiting the

application of relatively long duration on-line analyses (e.g., digitization of signals by CCDs) to only the data which satisfied cruder levels of filtering, such a system permitted the necessary level of sophisticated analysis without increasing system deadtimes to unmanageable levels. The first level trigger was a simple coincidence between the detection of a beam pion interaction in the target ($S1 \cdot S2 \cdot S3 \cdot \overline{S4}$) and a candidate neutron in the neutron bars. The typical rate for this trigger was ~2.3 kHz for π^- operation and ~1.2 kHz for π^+.

The second-level trigger which selected those events associated with a candidate stopped positive pion, searched for the characteristic decay: $\pi^+ \rightarrow \mu^+ \nu$ within the target. It was formed by comparing the normalized outputs of the ''short''- and ''long''-gated ADC's connected to the active target scintillators, using dedicated LeCroy ECLine trigger modules, with an excess signal in the long-gated ADC indicating a candidate stopped π^+. The time required for this trigger decision was 10 μs. By this means, the data rate was reduced to ~75 events/s for the π^- runs and ~60 events/s for the π^+. The second-level trigger is described in greater detail by Raywood *et al.* [12]. The computer live time of the experiment was evaluated by separately counting the triggers presented to the data acquisition system and the triggers processed by the system. The ratio of the two numbers gave the relative live time of the experiment, typically 85%.

As 93% of the incident pions did not interact in the target, beam events containing two or more pions almost always fired the veto scintillator, *S*4. Therefore the incident beam count had to be corrected to eliminate the contribution from multiple particle buckets (consisting of approximately 3.5% of the pions delivered to the target for a beam rate of ~1.7 MHz). As the beam rate varied somewhat during the experiment, the actual fraction of beam buckets containing more than one pion was determined during the individual runs using the appropriate Poisson statistics. Overall, ~96% of the beam bursts contained only one particle. Events containing two pions in one beam burst were vetoed by the *S*4 scintillator with 93% efficiency, this inefficiency arising because 7% of the beam pions interacted in the target.

For an average pion beam rate of 1.7 MHz, the cyclotron RF frequency of 23 MHz implied that ~7% of the pions delivered to the target were followed by a second pion in the next beam ''bucket'' 43 ns later. As the time required to search the target for a $\pi \rightarrow \mu \nu_{\mu}$ decay was more than 80 ns long, however, incident pion sequences of this type had to be rejected. This was accomplished by requiring ''acceptable'' events to be those associated with a single pion with no other pion following or preceding it by a period of at least 80 ns. Staightforward hardware coincidence logic [16] was used to perform this function. The overall fraction of acceptable beam burst events were evaluated for each run separately and averaged over the total data set for each energy and beam polarity; values ~92% were typical. The imposition of the above two constraints resulted in the loss of 15% of the $S1 \cdot S2 \cdot S3$ triggers.

D. In-beam and target scintillators

Pulse-height calibrations of the target and four in-beam scintillators were carried out using pions that stopped in the target as well as with those that traversed it completely (the energy loss of 200 MeV incident pions traversing the target was 1.3 MeV per 6 mm segment). An additional calibration appropriate to the target scintillators was provided by the 4.2 MeV muons from pion decay. For the latter calibrations, appropriate aluminum degraders were inserted into the beam to cause the incoming pions to stop in each of the target segments separately.

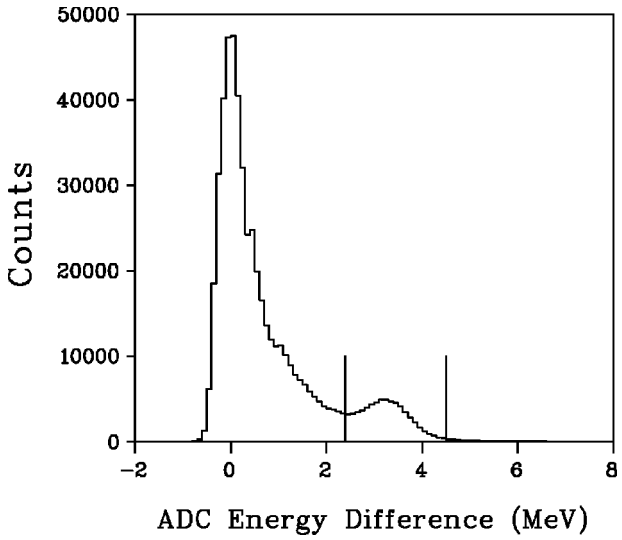

FIG. 4. Difference spectrum for the long and short gate ADC's associated with target segment *C*.

E. Stopped pion detection

The positive pions that were produced (and stopped) in the target were identified by their signature decay, $\pi^+ \rightarrow \mu^+ \nu_{\mu}$. Three different techniques were employed to identify and measure the height and relative time of occurrence of all pulses in each of the target segments for a period of 80 ns following the initial pion pulse [12].

The first technique, provided by coincidence circuitry fed by the discriminators attached to the target segment photomultipliers, was used both for diagnostic purposes during data taking and in the off-line analysis. It consisted of a ''hardware circuit'' [16] to detect the presence of a secondary pulse in a target segment within a time interval of 70 ns following the arrival of the incident pion. The second method, used in the second-level trigger, employed charge integrating ADC's with long and short gates as described earlier. A nonzero difference between their normalized ADC values indicated the presence of a second pulse. A typical example of such a difference spectrum is shown in Fig. 4 for target segment *C*. In addition to secondary pulse detection, this method also provided a measure of the energy of the extra pulse, as indicated in Fig. 4 by the small peak at ~4 MeV arising from the decay muons stopping in the scintillator.

The third and most powerful technique utilized 500 MHz transient digitizers developed at TRIUMF [13]. For each target section, these digitizers not only identified the presence, but also measured the pulse height and relative time of oc-

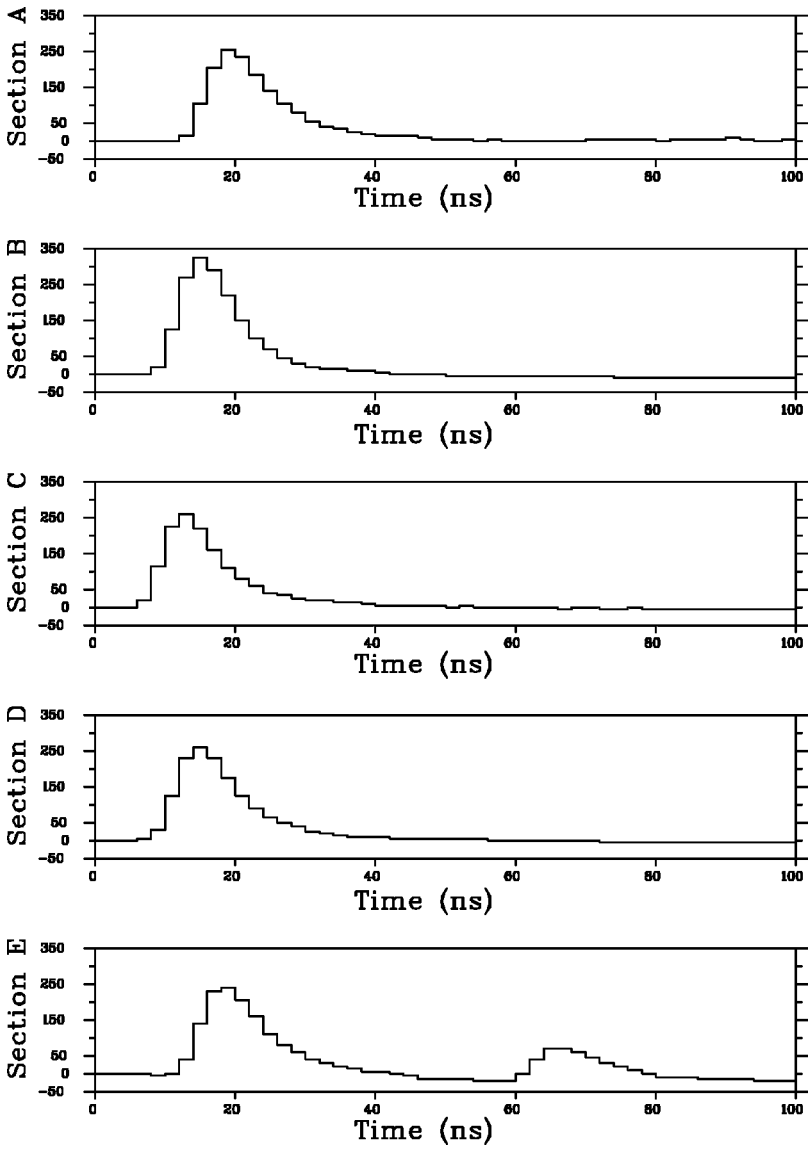

FIG. 5. Digitized ADC signals for each target segment arising from a typical event. In this case, a pion traverses the target and then decays to a muon in the final segment, Section E. The vertical scales are raw ADC units.

currence of all pulses which followed the initial pulse [12]. The array of digitizer signals characterizing a typical event associated with a pion decay in target segment *E* is shown in Fig. 5.

Off-line fitting of each pulse in such a pulse train to the pulse shapes characterizing pions traversing the whole target without interaction, enabled the pulse heights and relative time delays between all the significant signals to be determined (see Fig. 6). The resulting energy resolution of the muon peak was found to be $\pm\sim 0.6$ MeV, limited both by the inherent resolution of the CCD camera signals and the photon statistics at the phototubes.

The time of occurrence of the secondary pulse relative to the first was histogrammed for those pulses identified as muons. Figure 7, obtained for a run involving 200 MeV incident pions, is a typical example of such a spectrum. The fitted meanlife of 26.4 ± 0.5 ns is in good agreement with the accepted value of 26.0 ns for the charged pion lifetime. The useful region of the timing spectrum in Fig. 7 is indicated by the timing cut. This range was limited by both the triggering circuits and fitting routines, as it was not possible to reliably fit two peaks occurring within 10 ns in the CCD data. To reduce the number of background events detected, the final analysis involved the placement of cuts on the height of the second pulse, as shown in Fig. 6, as well as on its timing relative to the first pulse, as shown in Fig. 7. In addition, the ADC energy difference signals were required to be within the gate shown in Fig. 4.

F. Pion detection efficiency

The success of the experiment relied critically on knowledge of the stopped pion detection efficiency, η_π. This efficiency was determined by degrading $T_\pi = 30$ MeV pions from *M*11 using selected thicknesses of aluminum so that the pions were stopped in each of the target elements in turn. Application of those muon decay criteria discussed above to the CCD pulse heights and times of occurrence of the pulses associated with these beam sample pion events yielded η_π values which were typically $42\pm 2\%$ for all of the five active target segments.

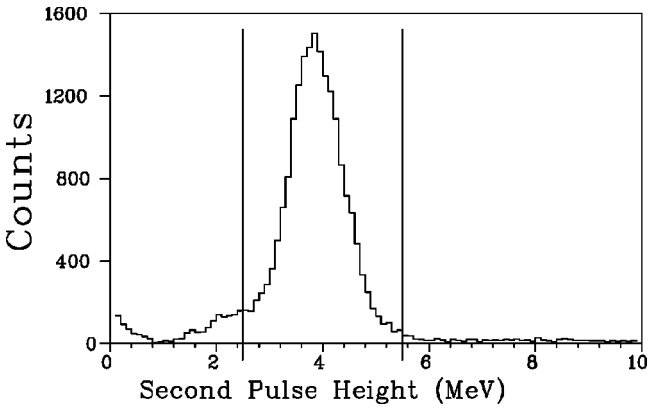

FIG. 6. Calibrated pulse height for muon candidates in target Section E. The gate used to identify muons is indicated by the vertical lines.

G. Neutron detection

As the first-level event trigger required the detection of a neutron (observation of a neutron signal from each end of one of the bars), reliable cross section determination required a thorough knowledge of the operational characteristics of the neutron detection array, a system consisting of a double hodoscope of fourteen scintillating bars. The bars, each of dimension $15\times15\times105\,\mathrm{cm}^3$, were arranged in two back-to-back stacks of seven bars each. A photomultiplier tube, feeding a TDC and an ADC, was mounted at each end of every neutron bar. Neutron energies were determined from their times-of-flight (TOF) from the target to the neutron bars. In addition, comparison of the timing information from each end of a given bar yielded a measure of the lateral position of the neutron detection.

The neutron detection efficiency, η_n, which depended on the energy deposition in the detection array, was determined using monoenergetic neutrons of 8.9 and 68 MeV, together with an appropriate model of the system in order to interpolate between these energies. These monoenergetic neutrons whose energies spanned the range of neutron energies available to the $\pi p\rightarrow\pi\pi n$ reaction were produced by stopping

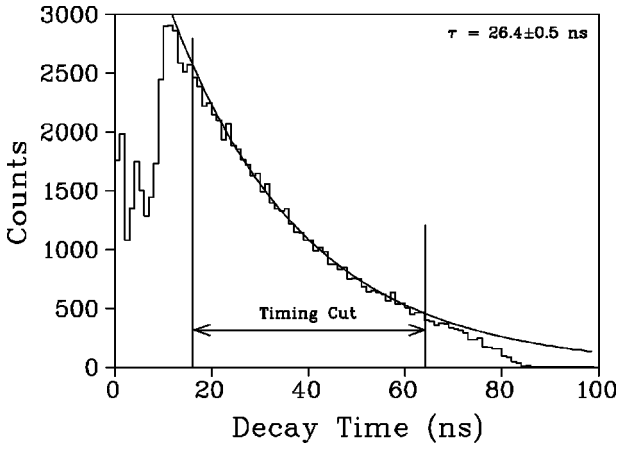

FIG. 7. Aggregate relative time distribution between primary and secondary (muon) pulses, summed over all target segments, for 200 MeV incident pions.

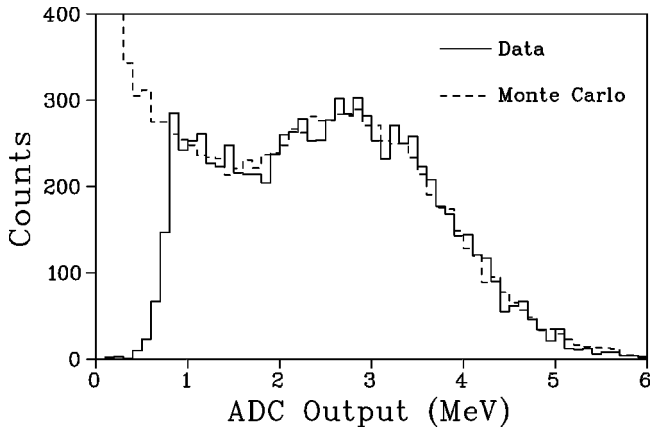

FIG. 8. A comparison of experimental data (solid line) with Monte Carlo simulation (dashed line) for one of the front neutron bars when bombarded with 8.9 MeV neutrons. A 0.13 MeV photon threshold is assumed.

negative pions in either liquid H_2 or D_2 cryogenic targets. The $\pi^-p\rightarrow\gamma n$ reaction in the hydrogen target provided 8.9 MeV neutrons, whereas the $\pi^-d\rightarrow nn$ reaction in the liquid deuterium target yielded 68 MeV neutrons.

Calibration of the time-to-digital converters connected to each end of the neutron bars was carried out using the 8.9 MeV neutrons and verified with the 68 MeV data [16]. The standard deviation in the determination of the 8.9 MeV neutron energy was 4%, corresponding to a FWHM of the TOF spectra of 3.4 ns, a value resulting from the flight time of the neutrons through the thickness of the scintillator bars. This TOF calibration was also consistent with the location of the γ peak present in the 8.9 MeV neutron TOF spectra. A similar TOF analysis for the 68 MeV neutrons yielded a neutron energy uncertainty of $\pm7\%$.

As it was important to know the detection efficiency of the neutron bars as a function of both the neutron energy and the value of the energy cut imposed on the neutron pulse height spectra, the necessary interpolations between the two calibration energies were carried out using a Monte Carlo code developed for NE-102 scintillator by Paticchio *et al.* at Kent State University [17]. The main input to the code involved (i) the effective number of photoelectrons per MeV of ionization energy and (ii) the ionization energy threshold for neutron detection. The 8.9 MeV neutrons exhibited a clean edge at the upper end of their pulse height spectra, an edge which corresponded to *np* elastic scattering with the proton acquiring all the kinetic energy of the neutron. Computer simulations carried out for ''energy per photon'' levels ranging from 0.01 to 0.24 MeV indicated that the simulated response curve corresponding to a photon threshold of 0.13 MeV most consistently reproduced the shape and position of the upper end of the pulse-height spectrum obtained for each element of the neutron bar array. A sample neutron ADC distribution for the 8.9 MeV neutrons is shown in Fig. 8 together with the Kent State Monte Carlo prediction appropriately scaled in counts to the data. The disagreement at low values of the ADC output is simply a result of instrumental thresholds. The neutron detection threshold subsequently selected for the experiment by means of a software cut (for all

bars) was 5 MeV, a value which minimized effects of noise without appreciably impacting the neutron detection efficiency.

The neutron detection efficiency, η_n, was obtained using

$$\eta_n = \frac{n_{\text{detected}}}{\pi_{\text{stopped}} P_f \Omega \Lambda}, \tag{3}$$

where n_{detected} is the number of neutrons detected over the software threshold, π_{stopped} is the number of negative pions which stopped in the target, P_f is the branching ratio for the reaction, Ω the solid angle subtended by the bars, and Λ is the fractional livetime of the data acquisition system, typically $\sim$95%.

π_{stopped} was determined by counting the number of pions which triggered $S1$, $S2$, and $S3$ but failed to trigger the veto scintillator, $S4$. The branching ratio, P_f, for $\pi^- p \rightarrow \gamma n$ is $39.0 \pm 0.3\%$ [18], whereas that for $\pi^- d \rightarrow nn$ is $73.7 \pm 0.3\%$ [19]. The solid angle subtended by each neutron bar was determined geometrically from the dimensions of the bar together with its distance from the target. Typical values were 15 msr for the front bars and 14 msr for the back. Although a neutron threshold of 5.0 MeV was used in the experiment in order to optimize the signal-to-noise ratio, a threshold of 1.9 MeV was used for calibration purposes due to the small fraction of events in the spectrum of Fig. 8 with energies in excess of 5.0 MeV. For example, for the lower 1.9 MeV threshold, the back bars detected 7.3% of the 8.9 MeV neutrons whereas only 0.15% was expected for the 5 MeV threshold. The detection efficiencies characterising the 1.9 MeV threshold are shown in Fig. 9 as a function of energy for the Monte Carlo simulation together with the experimentally determined values at 8.9 and 68 MeV. The average neutron detection efficiency for the front and back planes of the middle ten bars are compared to the Kent State Monte Carlo predictions in Table I. Due to the uncertainties in the cross-section data used in the code, an uncertainty of 10% was assigned to the predicted values. The extremely good agreement between the Monte Carlo predictions and the experimental data illustrates the level of reliability of the Kent State code for modeling these detection efficiencies. Of particular significance is the fact that the code correctly reproduced the detection efficiency of the back bars an indication that the code satisfactorily accounted for the neutron absorption in the front bars.

A complication which affected only the data acquired for the π^- channel of the reaction (and not the π^+) was that arising from gamma rays striking the neutron bars thereby simulating neutron signals. These gamma rays were produced upstream of the target by the substantial electron contamination of the π^- beam, a contamination originating from the neutral pions produced at the primary pion production target within the external proton beam of the cyclotron.[1] Gamma rays produced by these electrons could Compton scatter in the experimental target and subsequently strike the neutron bars, thus mimicking the signals produced by the neutrons from the target. This effect was of particular concern when produced by electrons in a beam burst following the beam bucket containing a pion, since this timing was indistinguishable from legitimate neutron signals. This background could be substantially eliminated, however, by applying appropriate cuts to the experimental data. Signals originating from electrons in the following beam burst were readily identified by examining histograms of the time of occurrence of the second fitted CCD pulse relative to the time of the first fitted CCD pulse, as shown in Fig. 10, and also histograms of neutron TOF from the target to the neutron bars as illustrated in Fig. 11. In both spectra the prominent peak occurring after a delay of approximately 40 ns corresponds to signals associated with the arrival of a par-

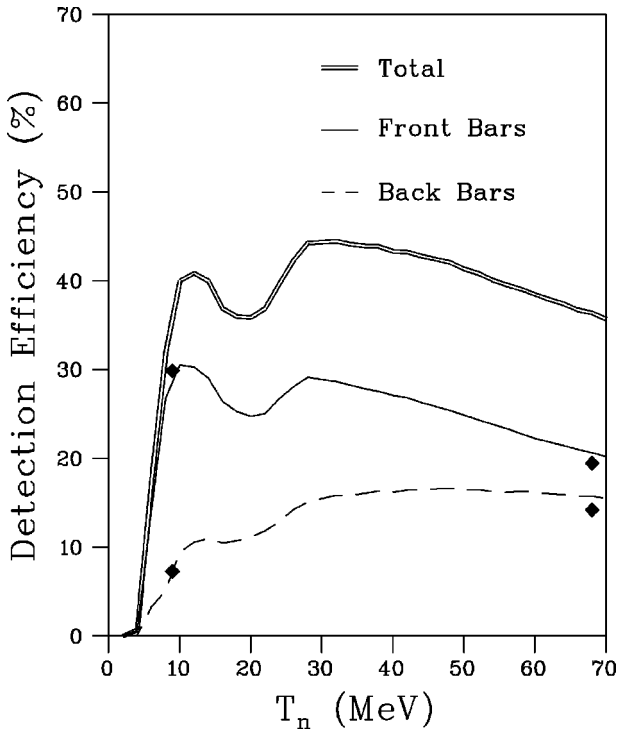

FIG. 9. Neutron detection efficiency of both the front and back neutron bars as a function of kinetic energy for a neutron detection threshold of 1.9 MeV. The curves describe the Kent State Monte Carlo prediction while the points at 8.9 and 68 MeV were determined experimentally. The errors are smaller than the size of the symbols.

TABLE I. Comparison of the neutron detection efficiency (NDE) with the Kent State Monte Carlo code predictions based on a neutron detection threshold of 1.9 MeV.

T_n (MeV)	Neutron bars	Kent State NDE predictions (%)	Measured NDE (%)
8.9	Front	29.6 ± 3.0	29.9 ± 0.4
	Back	7.3 ± 0.7	7.3 ± 0.2
68	Front	20.2 ± 2.0	19.4 ± 0.2
	Back	15.0 ± 1.5	14.1 ± 0.2

[1]The ratio of π^0/π^- is approximately seven times greater than for π^0/π^+.

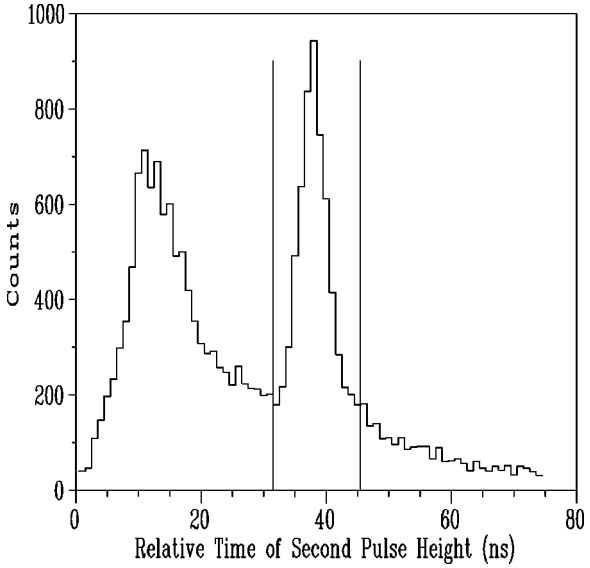

FIG. 10. Relative time of second fitted CCD pulse in target segment *D*, for a pion beam energy of 190 MeV. The timing gate is shown by the vertical lines.

ticle from a following beam burst. In order to reject such events from subsequent analysis, a cut was imposed upon the scatterplots of the time of the second target pulse versus neutron TOF for each target segment, a typical example of which is shown in Fig. 12. The photons are indicated by the dense patch of dots in Fig. 12. Use of the elliptical box gate shown in the figure facilitated rejection of the unwanted events without unduly discriminating against real events. The dashed line shown in Fig. 11 is the result of applying such a cut. Although not all of the background was removed, the loss of real events was minimal.

H. Experimental acceptance

The experimental acceptances, $\Pi(\eta_{\pi};\eta_{n};T_{\pi})$ for the reaction were determined using a Monte Carlo simulation of the experiment. This code tracked a pion into the target, generated an event randomly within the target, calculated overall phase space factors (using three-body phase space), and then tracked the resulting particles, determining whether

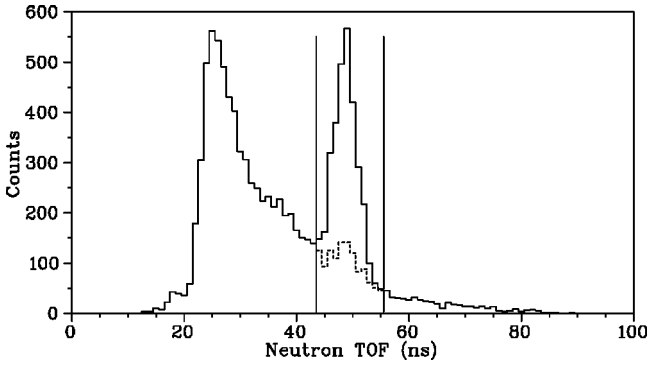

FIG. 11. Neutron TOF histogram for a pion beam energy of 190 MeV. The dashed line is the data after application of the elliptical box gate shown in Fig. 12.

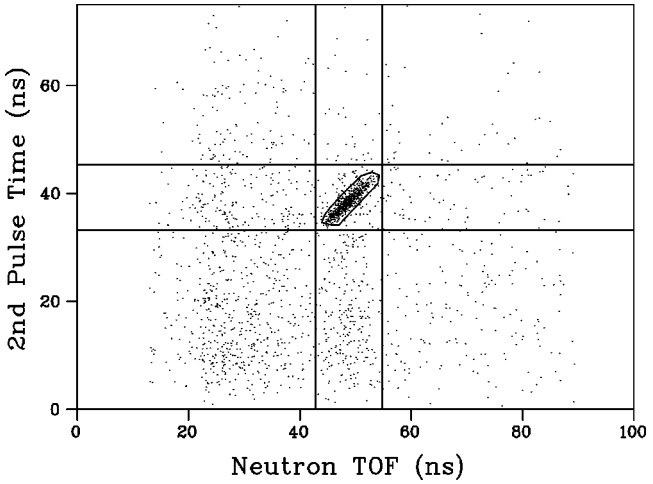

FIG. 12. Scatter plot of time of second CCD pulse in target segment *D* versus neutron time-of-flight for an incident π^{-} beam of 190 MeV pions. The gates shown in Figs. 10 and 11 are shown, as well as the elliptical box gate used in the analysis.

all of the detection criteria had been satisfied. The neutrons were tracked to the midplane of the neutron bar array where, in order to be detected, they had to satisfy the detection efficiency predicted by the Kent State Monte Carlo code for neutrons of that energy. Product pions were tracked until they stopped in (or left) the target. While within the target, energy losses were calculated using the Bethe-Bloch equation [20]

$$\frac{dE}{dx}=\frac{4\pi N_{A}z^{2}e^{4}}{mv^{2}}\frac{Z}{A}\left[\ln\left(\frac{2mv^{2}}{I(1-\beta^{2})}\right)-\beta^{2}\right] \tag{4}$$

and light deposition (after each step) using Birk's equation [21]

$$\frac{dL(E)}{dE}=\frac{S}{1+kB\dfrac{dE}{dx}} \tag{5}$$

to account for the quenching of the light output near the end of the track of a charged particle. E is the kinetic energy of the charged particle, L the light output of the scintillator, dE/dx the energy loss as calculated by the Bethe-Bloch equation, S a normalization constant, and kB is effectively a constant, determined by Rozen *et al.* [22] to be 0.0114 cm/MeV. The muons, produced by pions decaying in the target, were emitted over a 4π solid angle in the lab frame, with a mean lifetime of 26.0 ns. They were also tracked until they stopped in (or left) the target. The total energy (T_{sum}) deposited in the target by the incident pion, product pions and any decay muons, together with the kinetic energy of the associated neutron were recorded on an event-by-event basis.

In the case of the $\pi^{-}p\rightarrow\pi^{+}\pi^{-}n$ reaction where one of the final state pions was negatively charged, tracking of the negative pion was carried out in the same way as for the π^{+} (until it stopped in or left the target). However, instead of undergoing muon decay as was the case for the π^{+}, the negative pion was assumed to be absorbed by a carbon

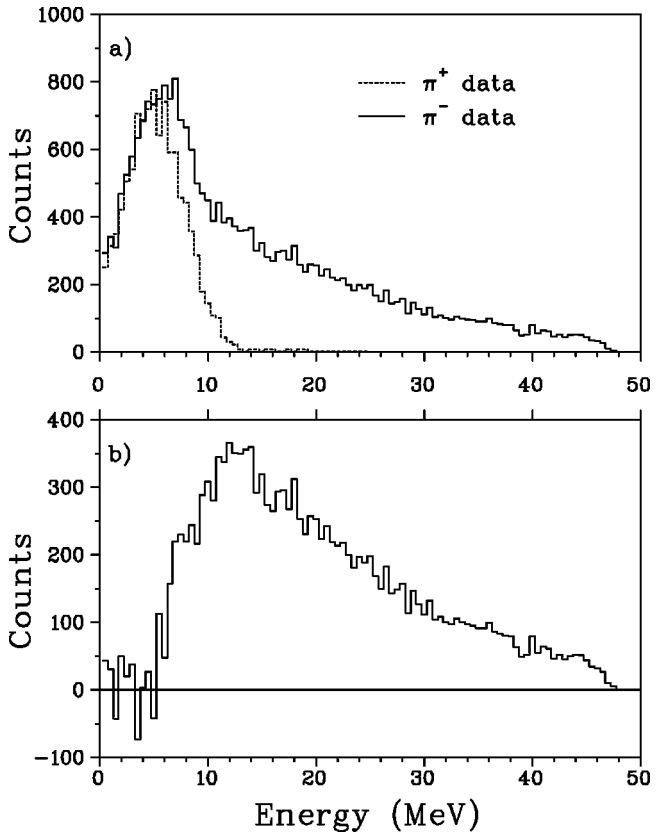

FIG. 13. Histograms used in the study of the energy deposited in the target due to carbon star formation. (a) Stopped π^- data and scaled stopped π^+ data. (b) Stopped π^- data with the scaled π^+ subtracted.

nucleus. In approximately 50% of such cases, the π^- absorption caused the carbon nucleus to explode, producing a star. However, in the the other 50%, the resulting nuclear reaction was characterized by the emission of two energetic neutrons together with a low energy residual nucleus. Since neither of the neutrons had a significant probability of interacting with the target, these events were also characterized by a constant value of $T_{\rm sum}$, and were those that constituted the events used in the determination of the yield of the reaction for the π^- channel. The other 50% of the cases, those producing stars, were indistinguishable from background since their values for $T_{\rm sum}$ were very poorly defined.

In order to obtain an experimental understanding of the carbon star effect, including its energy spectrum, two sets of data were compared, one set obtained using positive pions stopped in each target segment, and one using negative pions. Typical histograms of the energy deposit obtained for these cases is shown in Fig. 13.

For the positive pions, a well-defined peak occurs at the energy corresponding to the sum of the the kinetic energy of the decay muon and the stopping energy of the incident pion. In the case of the negative pions, however, a skewed peak occurs at the energy corresponding to that of a stopping pion but with a higher energy tail due to the energy released by a carbon star.

The positive pion energy spectra, after first being corrected for the average energy deposited by a stopping muon in a target segment, were normalized by scaling them (by a least squares fit) to the first 5 MeV of the negative pion spectra. The normalized positive pion spectra were then subtracted from the stopped energy spectra of the negative pions. The shape of the resulting energy distribution, used in the $\pi^- p$ analysis by the Monte Carlo code to account for the extra energy deposited in the target by a carbon star, is shown in Fig. 13(b). From such fits, it was found that 47.5 $\pm 0.9\%$ of the $\pi^- C$ interactions were ''starless,'' corresponding to the emission of neutrons leaving the daughter nucleus with negligible kinetic energy while the other 52.5% were associated with the significant energy release expected from a carbon star.

The Monte Carlo code used in this analysis was adapted from that originally written by Sevior [4] for the π^+ channel of the reaction, but expanded for the current experiment to account for the carbon stars produced by the absorption of negative pions in the target. Because of the energy loss suffered by the incident pions in the target (up to 6.6 MeV for pions whose kinetic energy is within 30 MeV of reaction threshold), a relatively large range of interaction energy characterises the reaction. Sevior's technique for extracting the energy-dependent cross-section, an energy dependence determined primarily by phase space, involved simulating the experiment in terms of an assumed production cross section (of arbitrary value) at the front face of the target. As the pions lost energy while traversing the target the cross section was reduced by an appropriate factor, one which included the dominant phase space dependence on energy. The total number of events expected, with all kinematic cuts, efficiencies, etc., incorporated into the code, was then determined on the basis of an incoming beam of 10^{12} pions. By comparing this result to the actual number of events recorded in data runs for this number of incident pions, the experimental value of the cross section was readily obtained.

As the maximum energy loss suffered by the incoming pions in the target was $\sim$6.6 MeV, it was found convenient to subdivide the target into 66 sections, each 0.1 MeV wide in terms of energy deposit. For each section, an event weighting factor, $T^{*2}\Phi$ [23], was recorded, where T^* was the energy above threshold (MeV) in the lab frame, and Φ accounted for the loss of particle flux while traversing the target. Since scaler data indicated that approximately 91% of all pions incident upon the target suffered no interaction, Φ was taken to vary linearly between 1.00 in the front section and 0.91 in the rear section.

When considering stopping pions and muons, it was necessary to incorporate the nonlinear response character of a scintillator which characterises such slow-moving particles. For the on-line data analysis (and also when histograms were generated from the Monte Carlo ''data'' for comparison with the real data), the nonlinear scintillator response was approximated simply by assuming that the light output was linearly related to the energy loss of the particle, but with a nonzero offset. The required offset was obtained by requiring the event peaks to occur at the expected values of $T_{\rm sum}$. A single value of this offset correctly located the event peaks in the $T_{\rm sum}$ spectra for all energies of both pion charges, including both the one- and two-pion analysis methods for the π^+

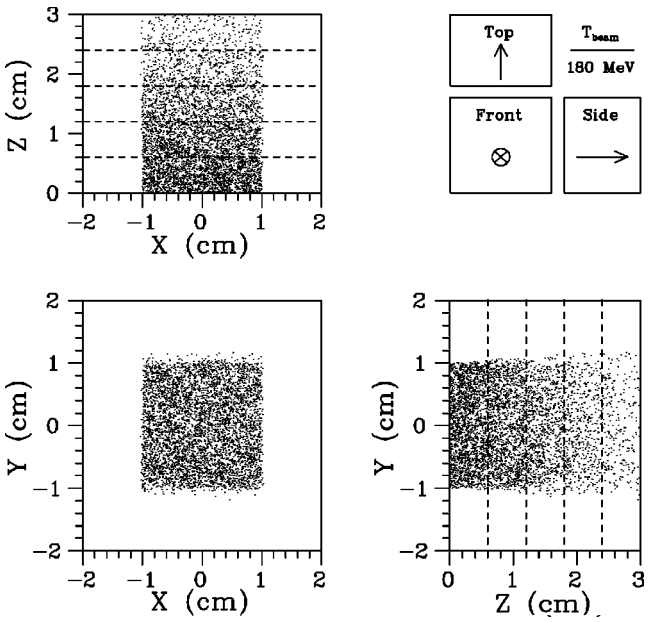

FIG. 14. Simulated location of initial beam interaction points within the target for $T_{\pi}=180$ MeV. The orientation of each face relative to the beam is shown in the upper right corner. Each target segment is indicated by the dashed lines.

channel. This applied to the analysis of the Monte Carlo generated data as well as to the analysis of the experimental data.

The depth of a $(\pi,2\pi)$ event within the 66 target sections was chosen in the usual Monte Carlo fashion using the weighting factor discussed above. The lateral position of an event was determined by the beam characteristics (see Sec. III B). As the event trigger required a signal from the square $S3$ in-beam scintillator, acceptable trajectories of the incident pions were those which illuminated a 2 cm$\times$2 cm region on the front of the target. When assigning appropriate random angles for the incident beam particles, they were of course required to also traverse the $S3$ scintillator. The momentum assigned to the pion was a value within the momentum spread observed in the experiment. A typical scatterplot of generated event locations within the target is shown in Fig. 14, a result of 5000 simulated events. The marked reduction in event generation as a function of z illustrates the decrease in cross section associated with traversal of the target due to the strong energy dependence of the reaction. When the location of a $(\pi,2\pi)$ event was selected, the Monte Carlo program then initiated the GEANT 3-body event generator [24] to produce two pions and one neutron isotropically in the center-of-mass frame. These were then Lorentz boosted to the laboratory frame. As a result, the pions as well as the neutron were conically distributed about the incident beam direction. The products of the simulated events were then tracked and subjected to the same acceptance tests as those imposed on the experimental data.

A typical simulated $T_{\rm sum}$ spectrum (for 200 MeV negative pions) is illustrated in Fig. 15. Clearly evident in the figure is the well-defined 2π peak comprised of the nonstar carbon events, a peak which was clearly evident as well in the experimental $T_{\rm sum}$ histograms.

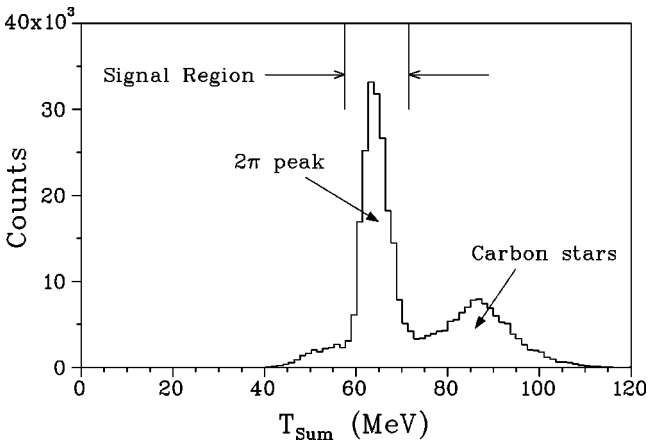

FIG. 15. Simulated $T_{\rm sum}$ spectrum characterizing bombardment by 200 MeV incident negative pions. The position of the gate used to extract the experimental yields is shown.

IV. π^+ CHANNEL RESULTS

A. Experimental yields

Each of the reaction channels, $\pi^+p\rightarrow\pi^+\pi^+n$ and $\pi^-p\rightarrow\pi^+\pi^-n$ were analyzed using the same methods of background estimation, yield extraction, and cross-section determination, with the experimental yields determined from the number of counts contained within the appropriate $T_{\rm sum}$ signal peaks.

Although weaker than the $\pi^-p\rightarrow\pi^-\pi^+n$ reaction by a factor of $\sim$5, the $\pi^+p\rightarrow\pi^+\pi^+n$ reaction benefitted from having both final state pions positively charged, thereby permitting free $\pi\rightarrow\mu$ decay for each pion. As a result, the appropriate $T_{\rm sum}$ spectra could be accumulated in two different ways. The first (''1π'' method) required the coincident detection of a neutron with the muon decay from only one of the stopped π^+ in the target. In this method, the substantial $\pi^+C\rightarrow\pi^+nX$ background was suppressed by constraining the acceptable kinematic ranges for $T_{\rm scin}$ and T_n to be within those expected on the basis of the Monte Carlo simulation of the $\pi^+p\rightarrow\pi^+\pi^+n$ reaction.

Since the dependence of the background reactions on incident energy was minimal over the energy range of consideration, the 172 MeV subthreshold data were used to provide the background information for both of the incident energies used for the $(\pi^+,2\pi)$ reaction, 184 and 200 MeV. These background 172 MeV spectra were subjected to the same experimental criteria (including kinematic restrictions for the T_n and $T_{\rm scin}$ parameters) as were the data. The background spectral shapes were scaled by simultaneously fitting them by least-squares to both the trailing edge (low energy) and to the 10 MeV wide region just above the peak of the signal spectra, as illustrated in Figs. 16 and 17. The extra signal events occurring at a $T_{\rm sum}$ value of $\sim$75 MeV in the 200 MeV one-pion difference spectrum reflects the inability of the scaled 172 MeV data to completely describe the higher energy region of phase space characteristic of the higher energy data. However, the ability of the scaled 172 MeV data to accurately represent the background to an energy at least 10 MeV above the location of the $(\pi,2\pi)$ signal peak justifies

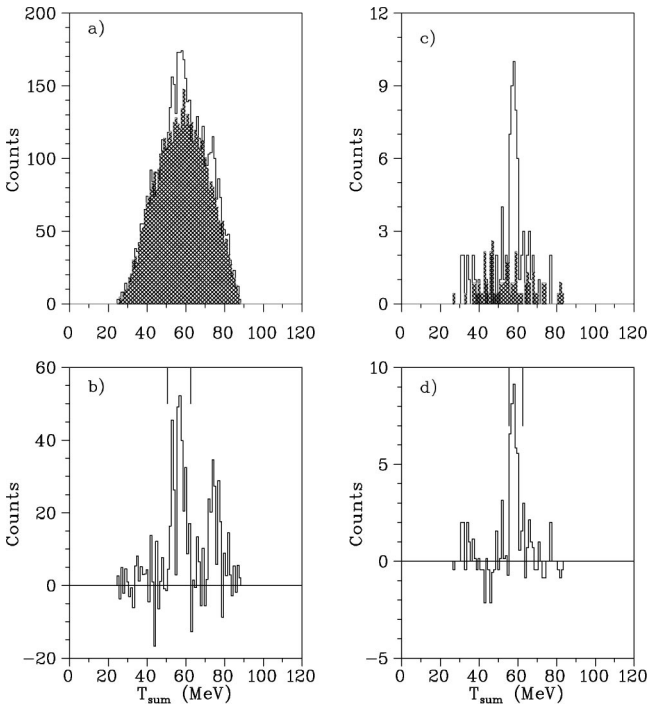

FIG. 16. $T_{\rm sum}$ spectra obtained for an incident π^+ beam of 200 MeV, together with fitted backgrounds, for both the (a) one-pion and (c) two-pion methods. The difference spectra for these methods are illustrated in (b) and (d), respectively. The regions used to extract the experimental yields are within the vertical markers.

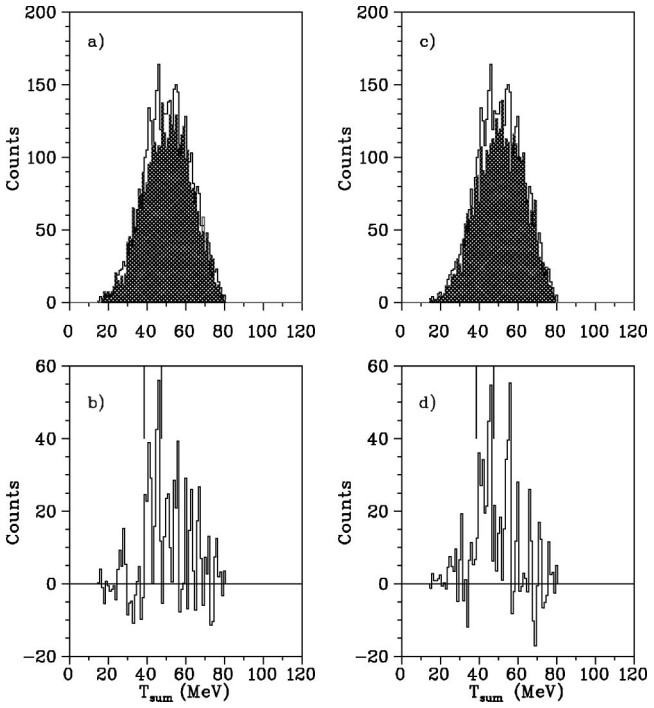

FIG. 17. $T_{\rm sum}$ spectra obtained for an incident π^+ beam of 184 MeV, together with fitted backgrounds, for both the (a) one-pion and (c) two-pion methods. The difference spectra for these methods are illustrated in (b) and (d), respectively. The regions used to extract the experimental yields are within the vertical markers.

the applicability of this method of determining backgrounds.

The second technique for extracting yields (''2π'' method) required the detection of two positive pions in the target, each stopping in a different target segment. As is evident in Figs. 16 and 17, this requirement of a second π^+ improved the signal/background ratio by almost an order of magnitude. The background $T_{\rm sum}$ spectra for the ''2π'' technique were obtained from the 172 MeV data by the same method as for the ''1π'' technique. The experimental yields were obtained by summing the counts within the signal peaks after subtracting the background. The width of the region around the peaks over which the sums were carried out, is indicated by the vertical markers in the relevant figures. In fact, these widths were varied to insure that all the signal was included.

When using the ''2π'' method for analyzing the π^+ channel, it was necessary to correctly account for intratarget drift of the muons. If a muon was generated near the interface between two target segments, it was possible for it to traverse the boundary and deposit some of its energy in each segment. Hence a single pion decay in the target could provide a pair of pulses in adjacent target segments, thus simulating a two-pion event. Such events were identified by monitoring the absolute time differences between muon pulses in adjacent target segments. A histogram of such timing differences for an incident pion beam of 200 MeV is shown in Fig. 18. Exclusion by means of a drift gate of events whose time difference was $\leqslant$3 ns eliminated approximately 40% of the events from the two-pion spectra. However, as indicated in Fig. 18(b), less than 10% of these events were contained within the $(\pi,2\pi)$ peak in the $T_{\rm sum}$ spectrum. Similar rejection rates characterized the 184 MeV data as well.

The experimental yields, provided by the number of counts in the signal peak region of each difference spectrum, are listed in Table II. The errors quoted for the yields reflect both the statistical uncertainty as well as the uncertainties inherent in the technique used for fitting the background.

The resulting cross-section values are listed in Table III. The numerical agreement between the ''1π'' and ''2π'' methods of analysis provides the most conclusive confirmation of the reliability of using the 172 MeV data as an appropriate description of the experimental background for this data.

B. π^+ channel cross sections

The experimental acceptances, $n_{tgt}\Pi(\eta_\pi;\eta_n)$, determined by the Monte Carlo simulation of the experiment, can be expressed in the form

$$n_{tgt}\Pi(\eta_\pi;\eta_n;T_\pi)=\frac{[GNBAR][PI][KIN][PEAK][f]}{[ID]}, \tag{6}$$

where n_{tgt} is the areal density of hydrogen atoms in each 0.1 MeV ''slice'' of the active scintillator target, $[GNBAR]$ is the probability of neutron detection based on observation of a clear signal from both ends of a bar, $[PI]$ is the probability of detection of the muon pulses in the target (for a single muon

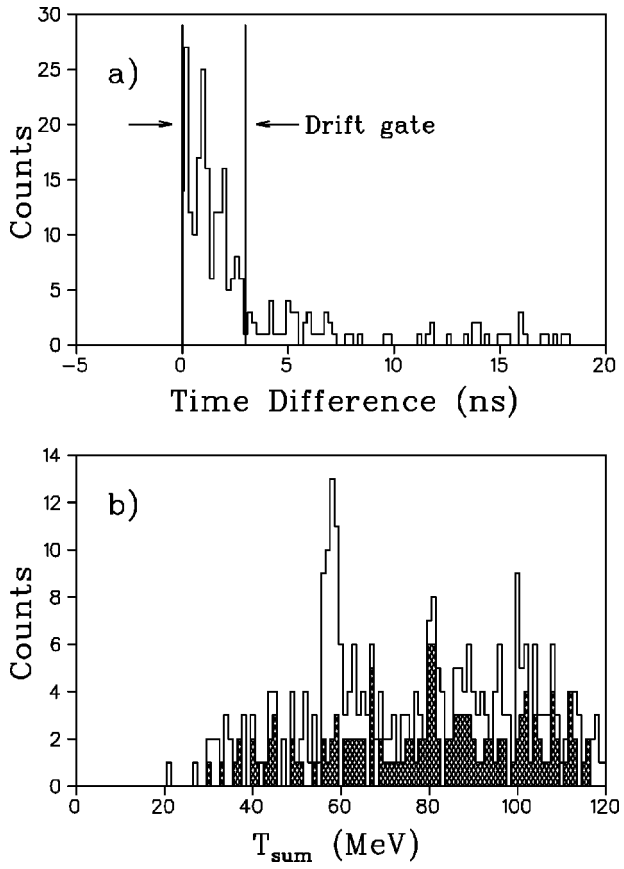

FIG. 18. The effects of intratarget drift of muons between adjacent target segments. (a) The absolute time difference between muon pulses in adjacent target segments for an incident pion beam of 200 MeV. (b) The corresponding $T_{\rm sum}$ spectrum (''2π'' method) without the drift correction (solid line). The $T_{\rm sum}$ background corresponding to detection of the two muon signals due to intratarget drift, corresponding to data for which the time difference was $\leqslant$3 ns, is indicated by the shaded region.

pulse for the ''1π'' technique and for both muons for the ''2π''), [*KIN*] is the joint probability that both the $T_{\rm scin}$ and T_n values are within the accepted ranges, [*PEAK*] is the number of events having a $T_{\rm sum}$ value within the signal peak, [*ID*] is the total number of events simulated and, for the ''1π'' technique, $f=1$. For the ''2π'' method, f is the fraction of simulated events for which the intratarget time difference is $>$3 ns.

Finally, the Coulomb corrected cross sections (in μb) were obtained from the experimental data using

$$\sigma=\frac{1}{n_{tgt}\Pi(\eta_\pi;\eta_n)}\frac{\mathcal{C}}{N_i\Lambda}\frac{Yield\times 10^{12}}{\mathcal{Y}}, \qquad (7)$$

TABLE II. Yields for the π^+ channel of the reaction for both ''1π'' and ''2π'' methods of analysis.

$T_{\rm beam}$ (meV)	One-pion	Two-pion
200	320±70	45±8
184	350±70	39±8

TABLE III. $\pi^+p\rightarrow\pi^+\pi^+n$ cross sections.

$T_{\rm beam}$ (MeV)	Cross section (μb)		
	One-pion	Two-pion	Average
200±1	1.4±0.4	1.4±0.3	1.4±0.3
184±1	0.30±0.07	0.30±0.07	0.30±0.07

where N_i denotes the number of pions incident upon the target, Λ is the fractional CPU livetime of the data acquisition system, Yield is the experimentally determined yield satisfying the kinematic cuts described earlier and $\mathcal{Y}$ is the expected Monte Carlo yield for 10^{12} incident pions assuming a 1 μb cross section at the front of the target. The Coulomb correction, $\mathcal{C}$, determined according to the prescription of Bjork *et al.* [6], amounted to 5% for the 200 MeV results, and 8% for the 184 MeV. The resulting values for the experimental cross sections are listed in Table III and displayed in Fig. 19.

The cross-section uncertainties listed in Table III were obtained by adding in quadrature the relative error due to each contributing factor, the values of which are listed in Table IV. $\sigma(n)$ and $\sigma(\pi)$ are the relative uncertainties associated with the detection efficiencies for the neutron and pion, respectively, σ(beam) is the relative uncertainty contributed by the energy-dependent factors ($\mathcal{Y}$, Π) of Eq. (7) due to error in determining the beam energy, σ(yield) is the relative error arising from statistical fluctuations in the yield and σ(syst.) accounts for the systematic uncertainties. The relative uncertainties in the neutron detection efficiency were set at 10% to reflect possible errors in the cross sections used in the Kent State Monte Carlo code. The uncertainties in the pion detection efficiency, 5% for the one-pion method and 10% for the two-pion method, were determined from the stopped pion data by comparing the number satisfying the timing cuts imposed on the pion decay timing spectra shown in Fig. 7 to the number stopped.

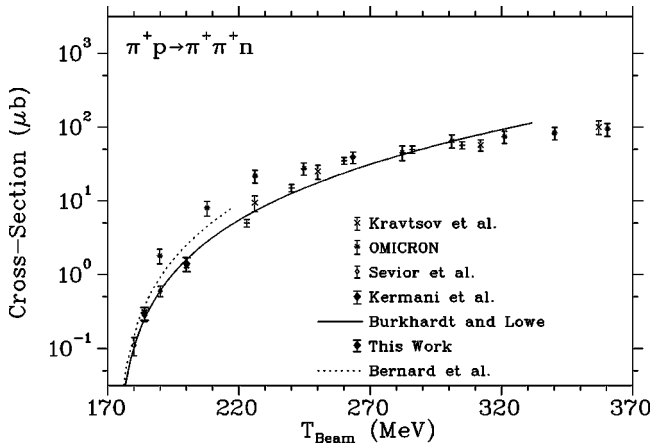

FIG. 19. Total $p(\pi^+,\pi^+\pi^+)n$ cross sections as a function of incident pion energy. The references for the data points are Kravtsov [3], OMICRON [5], Sevior *et al.* [4], and Kermani *et al.* [26]. The solid line is the phase shift result of Burkhardt and Low [7]. The dashed line is the theoretical prediction of Bernard *et al.* [11].

TABLE IV. Relative uncertainties of the individual components of the $\pi^+ p \rightarrow \pi^+ \pi^+ n$ cross-section determination.

T_{beam} (MeV)	Method	$\sigma(n)$	$\sigma(\pi)$	σ(beam)	σ(yield)	σ(syst)	σ(sigma)
200	One-pion	0.10	0.05	0.02	0.22	0.04	0.25
	Two-pion	0.10	0.10	0.02	0.16	0.02	0.22
184	One-pion	0.10	0.05	0.02	0.20	0.03	0.23
	Two-pion	0.10	0.10	0.02	0.18	0.02	0.23

Error in knowledge of the beam energy affected the phase space of the reaction, the strength of the Coulomb correction and the experimental acceptance. Since it thus contributed as a systematic uncertainty, its effect was evaluated by determining the overall conversion factor (Π) at 1 MeV above and below the central values, since this energy range encompassed the known spread in the beam energy [14] as well as the uncertainty in the calibration of the *M*-11 channel [25]. The resulting uncertainty in the cross sections due to the 1 MeV uncertainty in the beam energy was 2% for both the 200 MeV and 184 MeV data, an uncertainty significantly less than the uncertainty in phase space itself ($\pm$ 11% at 184 MeV) since the change in phase space was almost completely compensated by the associated change in the geometric acceptance of the system.

The uncertainties in the yields were determined using Poisson statistics applied to the signal and background counts within the selected regions about the peak. The cross section uncertainties, σ(syst.), arising from inadequacies in the choice of the kinematic energy ranges selected for the (π,2π) event cuts, ranges determined from the Monte Carlo studies, were evaluated by varying the gate widths of the relevant kinematic ranges. For T_π and T_n the ranges were varied by $\pm$ 4 MeV. For the case of T_{sum}, a variation of $\pm$ 2 MeV was used to obtain σ(syst.). The resulting relative variation in cross section is listed as σ(syst.) in Table IV. All the values quoted for the error contributions are consistent with those determined by Sevior *et al.* [4] in the earlier study of the reaction.

As is apparent in Fig. 19, these π^+ channel cross sections are in excellent agreement with those of Sevior *et al.* [4] but disagree with those of the OMICRON Collaboration [5].

V. π^- CHANNEL RESULTS

A. Experimental yields

Unlike the π^+ channel of the reaction for which two $\pi^+ \rightarrow \mu \nu_\mu$ decays occur, the π^- reaction channel yields only a single decay muon. Hence only the ''1π'' method of analysis was possible. As all the experimental calibrations required for the π^+ reaction channel were also relevant for the π^- channel (including thresholds and timing cuts used in the muon and neutron identification tests), elimination of the electron background was the only extra task required before yield extraction could be performed.

T_{sum} backgrounds for this channel were obtained using pions of both 172 and 176 MeV. Although 176 MeV is

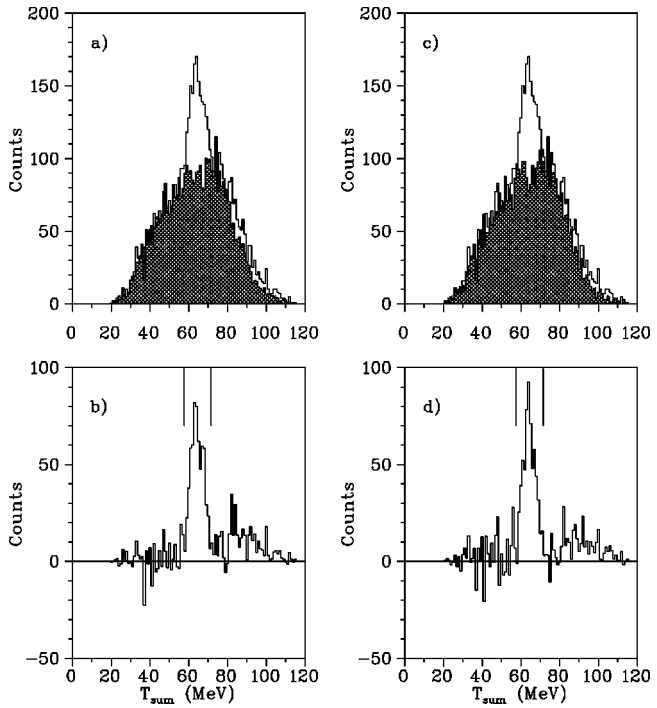

FIG. 20. T_{sum} spectra for incident π^- of 200 MeV. The (fitted) background data were obtained using (a) 172 MeV and (c) 176 MeV incident pions. The difference spectra are illustrated in (b) and (d), respectively. The regions used to extract the experimental yields are indicated by the vertical lines.

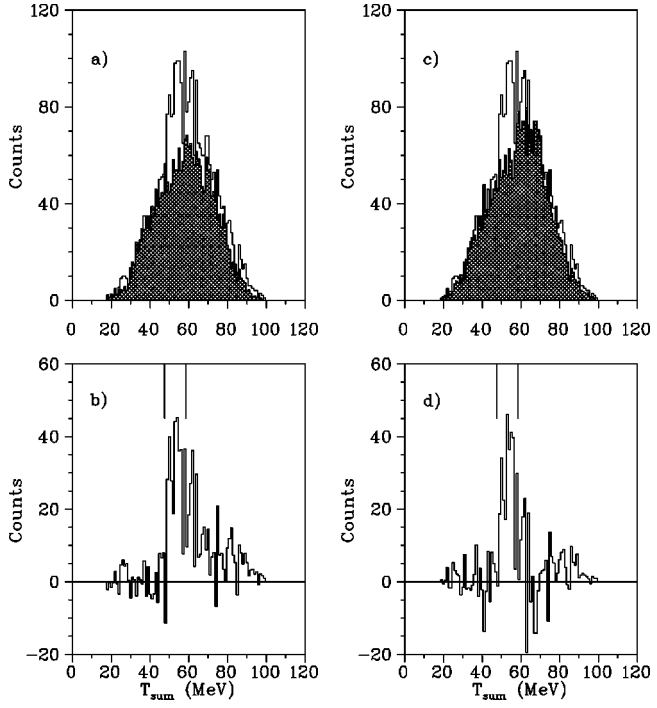

FIG. 21. T_{sum} spectra for incident π^- of 190 MeV. The (fitted) background data were obtained using (a) 172 MeV and (c) 176 MeV incident pions. The difference spectra are illustrated in (b) and (d), respectively. The regions used to extract the experimental yields are indicated by the vertical lines.

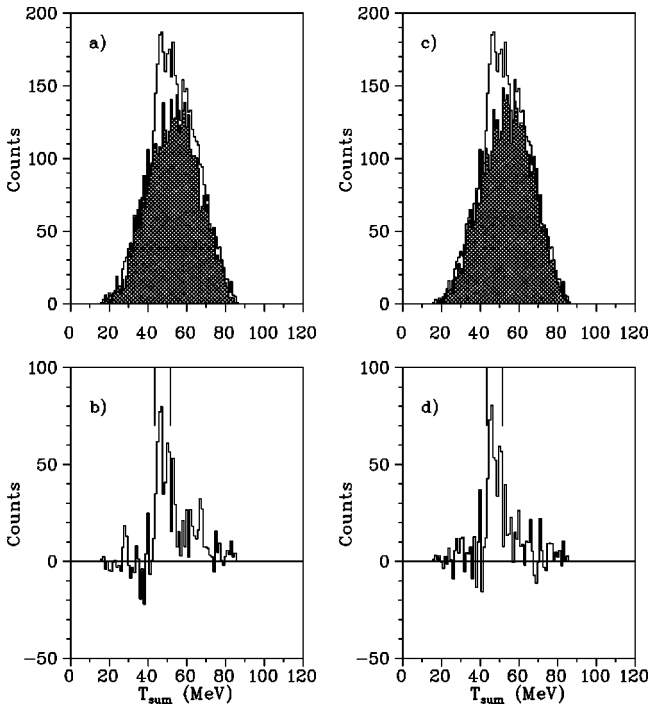

FIG. 22. $T_{\rm sum}$ spectra for incident π^{-} of 184 MeV. The (fitted) background data were obtained using (a) 172 MeV and (c) 176 MeV incident pions. The difference spectra are illustrated in (b) and (d), respectively. The regions used to extract the experimental yields are indicated by the vertical lines.

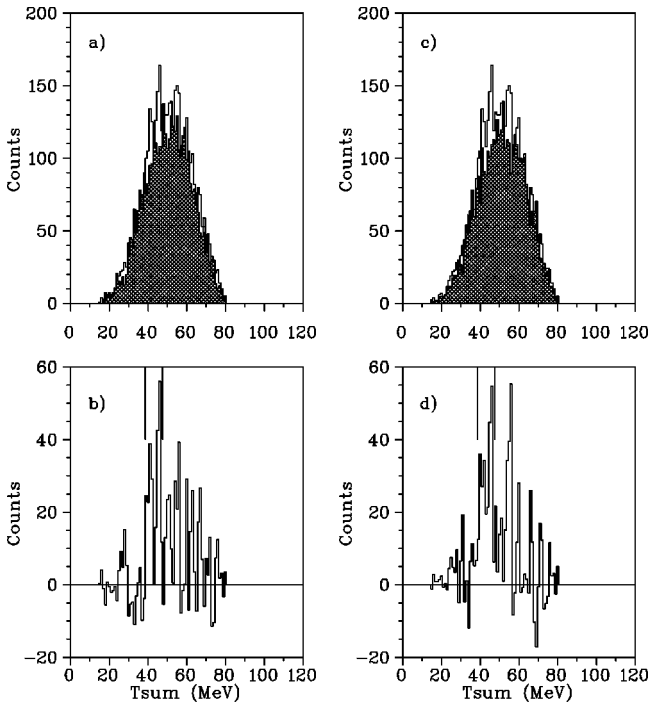

FIG. 23. $T_{\rm sum}$ spectra for incident π^{-} of 180 MeV. The (fitted) background data were obtained using (a) 172 MeV and (c) 176 MeV incident pions. The difference spectra are illustrated in (b) and (d), respectively. The regions used to extract the experimental yields are indicated by the vertical lines.

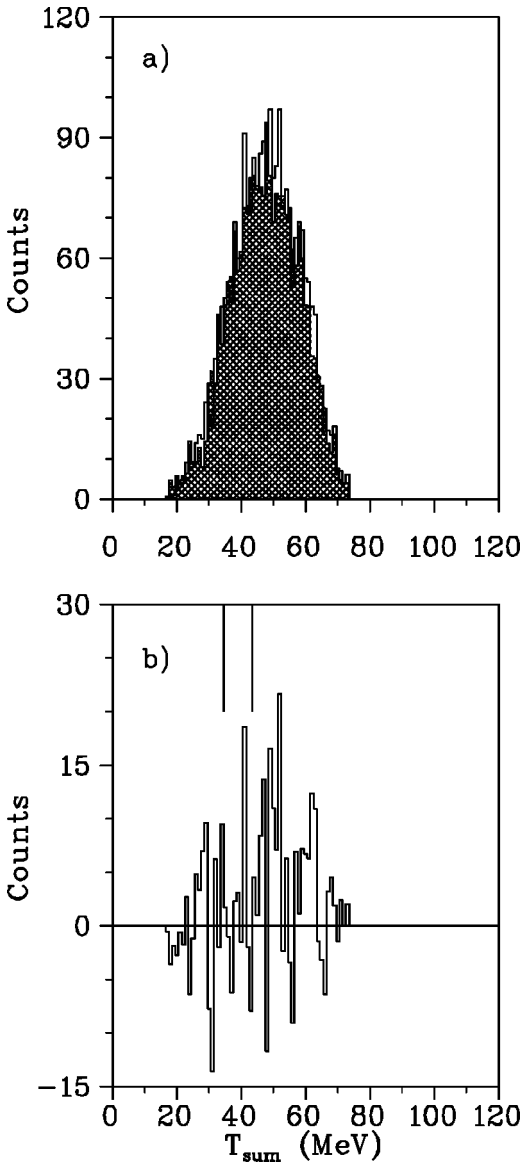

FIG. 24. $T_{\rm sum}$ spectrum for incident π^{-} of 176 MeV. The (fitted) background data were obtained using 172 MeV incident points. The difference spectrum is illustrated in (b). The region used to extract the experimental yields is indicated by the vertical lines.

above the threshold for the $\pi^{-}p\rightarrow\pi^{+}\pi^{-}n$ reaction, the yield at this energy was very small and was associated with $T_{\rm sum}$ values smaller than that appropriate for the beam energy of interest. As a result, the yields obtained using these two background approaches agreed within errors. Although only the ''1π'' method of analysis could be employed for the $\pi^{-}p\rightarrow\pi^{-}\pi^{+}n$ reaction, the signal to background ratio was much better than that associated with the ''1π'' method applied to the π^{+} channel as its cross section was about 5 times larger than that of the $\pi^{+}p\rightarrow\pi^{+}\pi^{+}n$ reaction. In addition, the background was lower since it was mainly due to double charge exchange on the ^{12}C nucleus. For this channel, the background spectra were only normalized to the trailing (low energy) edge of the signal spectra, again by least-square fits, because of the contribution of the carbon star events at higher energy. The final spectra (along with their fitted back-

TABLE V. Experimental yields (in counts) for the π^- channel of the reaction.

T_{beam} (MeV)	Background 172 MeV	Background 176 MeV	Combined set
200±1	632±52	616±56	625±54
190±1	278±30	289±32	283±31
184±1	397±42	451±54	418±48
180±1	127±33	182±35	155±34
176±1	16±12		16±12

grounds) are displayed in Figs. 20–24. In the spectra for beam energies above 172 MeV, the excess above background generated by the star events is clearly visible for T_{sum} energies above the monoenergetic peak. The similarity between the shapes of the difference spectra and those expected from the Monte Carlo simulation (Fig. 15) is readily apparent.

The energy ranges from which the experimental yields were extracted are illustrated by the vertical markers in the background-subtracted spectra of Figs. 20–24. The positions of these markers were determined from the Monte Carlo simulations. Table V presents the experimental yields (in counts) together with their statistical uncertainties (including that arising from the background fitting technique).

B. π^- channel cross sections

The experimental ''acceptance,'' Π, was determined from a Monte Carlo simulation in exactly the same way as was described for the ''1π'' positive pion channel analysis, except for imposition of the additional box cut filter used to exclude the false neutron signals resulting from the gammas produced by the electron contamination of the beam.

The cross sections were determined in exactly the same manner as for the positive pion channel, except, of course for inversion of the Coulomb correction. This correction varied from 15% just above threshold (at 176 MeV) to 5% at 200 MeV incident energy. The values for the cross sections are listed in Table VI and displayed in Fig. 25.

The various contributions to the error in the π^- channel cross-sections were determined in the same way as for the π^+ reaction channel. The values of these contributions are listed in Table VII.

VI. DISCUSSION

This experiment and that of the OMICRON Collaboration [5] are the only two which measured near-threshold values of the cross section for $\pi p \to \pi\pi n$ reactions involving both π^+ and π^- incident beams although only the data from our experiment are as close to threshold as 8 MeV. The data from these and other experiments were shown in Fig. 19 and 25. Although the larger cross-section values associated with the π^- channel obtained by both OMICRON and ourselves are in agreement (as well as with the data from other experiments), our lower cross-section π^+ results disagree with OMICRON but agree instead with those of Sevior [4]. These latter cross sections are sufficiently small that backgrounds constitute a serious problem. A major advantage of the current experimental technique is its ability to exploit ''2π'' detection for the π^+ channel in order to discriminate against many of these sources of background.

TABLE VI. Cross sections for the π^- channel of the reaction.

T_{beam} (MeV)	Cross section (μb)
200	6.54±0.91
190	2.99±0.48
184	1.85±0.27
180	0.74±0.11
176	0.18±0.14

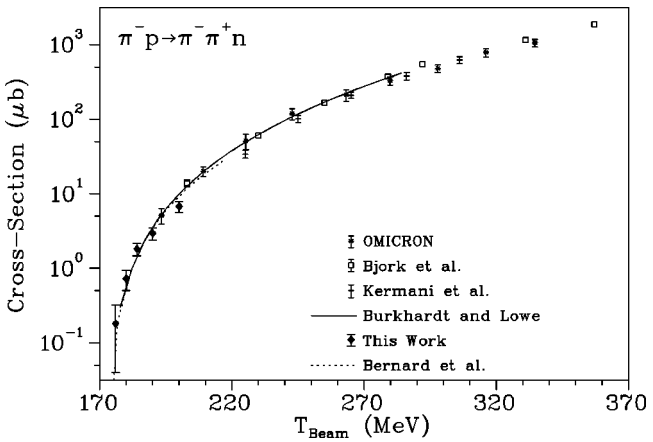

FIG. 25. Total $\pi^- p \to \pi^- \pi^+ n$ cross section as a function of incident pion energy. The data refer to the results of Bjork *et al.* [6], the OMICRON Collaboration [5], Kermani *et al.* [26], and this work. The solid line is the phase shift result of Burkhardt and Lowe [7], and the dashed line is the theoretical prediction of Bernard *et al.* [11].

A. Reaction amplitudes

Values for the $\pi\pi$ scattering amplitudes, $\mathcal{A}_{2I,I_{\pi\pi}}$, shown in Fig. 26 and 27, were obtained from our cross-section results by applying the formulation of Bernard, Kaiser, and Meißner [23,11]:

$$\sigma_{\text{tot}}^{\pi^+ p\to\pi^+\pi^+ n}(T_\pi) = 3.08\times 10^{-4}\ \mu\text{b}\,|\mathcal{A}_{32}|^2 (T_\pi - T_\pi^{\text{thr}})^2, \tag{8}$$

TABLE VII. Relative uncertainty of the individual components of the cross-section determination for the π^- channel of the reaction.

T_{beam} (MeV)	$\sigma(n)$	$\sigma(\pi)$	σ(beam)	σ(yield)	σ(syst)	σ(sigma)
200	0.10	0.05	0.03	0.03	0.07	0.14
190	0.10	0.05	0.07	0.06	0.07	0.16
184	0.10	0.05	0.06	0.05	0.07	0.15
180	0.10	0.05	0.05	0.06	0.07	0.15
176	0.10	0.05	0.02	0.75	0.07	0.76

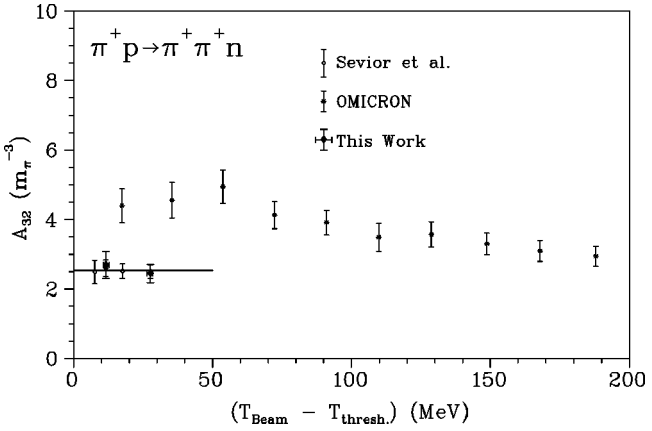

FIG. 26. $\mathcal{A}_{32}$ as a function of energy above threshold for Sevior *et al.* [4], the OMICRON Collaboration [5], and this work. The constant value has been fit to the data comprising the first 30 MeV above threshold (excluding OMICRON).

$$\sigma_{\rm tot}^{\pi^-p\to\pi^-\pi^+n}(T_\pi)=1.71\times10^{-4}\,\mu{\rm b}|\mathcal{A}_{10}-\mathcal{A}_{32}/\sqrt{10}|^2(T_\pi-T_\pi^{\rm thr})^2. \quad (9)$$

In the case of the $\pi^-p\to\pi^-\pi^+n$ reaction, Eq. (9) neglects the p-wave $I=1$ component, which, while it vanished at threshold, contributes at the measured energies. According to the phenomenology of HBχPT (heavy baryon chiral perturbation theory), the matrix elements are expected to be constant near threshold, so lines of zero slope were fit to the first 30 MeV region above threshold. For $|\mathcal{A}_{32}|$, the fit was made to the π^+ channel results of both this experiment and that of Sevior *et al.* [4]. The result, $|\mathcal{A}_{32}|=2.52\pm0.04\pm0.07(m_\pi^{-3})$, yields for the energy dependence of $\sigma_{\rm tot}^{\pi^+p\to\pi^+\pi^+n}(T_\pi)$ the broken line shown in Fig. 28. Values for $|\mathcal{A}_{10}|$ were obtained by inserting the above value of $|\mathcal{A}_{32}|$ into Eq. (9) with the relative phase difference between the two amplitudes neglected.[2] The zero slope fit to the results of the first 30 MeV above threshold yields a value of $8.5\pm0.4\pm0.4(m_\pi^{-3})$ for $|\mathcal{A}_{10}|$. The first value shown in the uncertainties is the contribution of the statistical fluctuations in the data while the second reflects the systematic uncertainty in the energy of the beam. This was determined by shifting all of the experimental data by $\pm$ 1 MeV, the uncertainty in the energy of the beam, and then repeating the whole data analysis in each case.

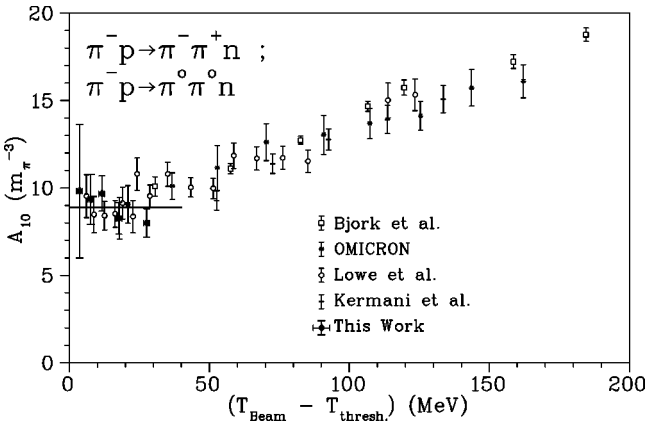

FIG. 27. $\mathcal{A}_{10}$ as a function of energy above threshold for Bjork *et al.* [6], the OMICRON Collaboration [5], Lowe *et al.* [27], Kermani *et al.* [26], and this work. The constant value has been fit to the data comprising the first 30 MeV above threshold.

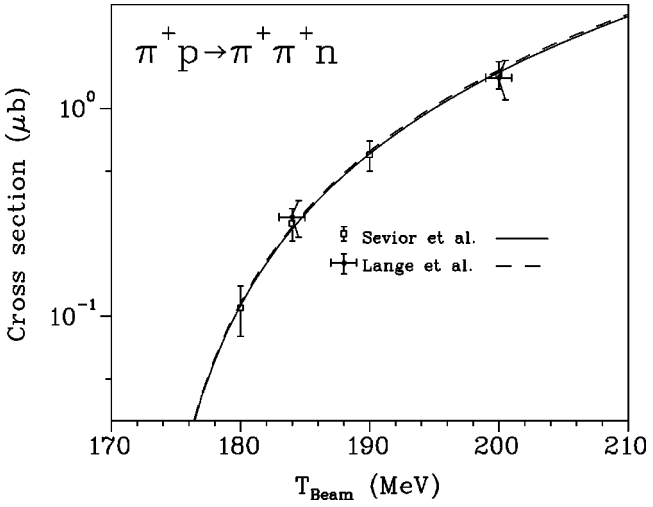

FIG. 28. Near threshold values of the total $\pi^+p\to\pi^+\pi^+n$ cross section. The data shown are only those of Sevior *et al.* [4] and our experiment.

Values for the $\pi\pi$ scattering lengths were obtained from the reaction amplitudes using the following expressions from Bernard, Kaiser, and Meißner [23,11]:

$$\mathcal{A}_{10}=25.05a_0+2.865\pm1.28, \quad (10)$$

$$\mathcal{A}_{32}=-35.58a_2+1.414\pm0.21. \quad (11)$$

Using the values for $|\mathcal{A}_{10}|$ and $|\mathcal{A}_{32}|$ described above, these yield $a_0=(0.23\pm0.08)m_\pi^{-1}$ and $a_2=(-0.031\pm0.008)m_\pi^{-1}$.

VII. CONCLUSIONS

The 1991 amplitude analysis of Burkhardt and Lowe [7] included all the data available at the time for the five channels of the ($\pi p\to\pi\pi n$) reaction. This analysis yielded an acceptable degree of consistency between all the published data sets above 250 MeV. However, a lack of consistency between the various sets of data nearer threshold required them to exclude the Omicron and Kravtsov data below 255 MeV in order to obtain a unique fit. Since it is the near-threshold values of an amplitude analysis that are required for determining the π-π scattering lengths and for enabling other tests of chiral perturbation theory, it is clearly impor-

[2]If the relative phase is the same as that of the elastic amplitudes, its neglect affects the value of $|\mathcal{A}_{10}|$ by less than 0.35%.

TABLE VIII. Comparison of theoretical and experimental values for the π-π scattering lengths. The uncertainties include both statistical and systematic errors.

Reference	$a_0[m_\pi^{-1}]$	$a_2[m_\pi^{-1}]$
Gasser and Leutwyler [28]	0.20 ± 0.01	-0.042 ± 0.002
Bijnens *et al.* [29]	0.2156	-0.0409
Girlanda *et al.* [30]	0.209 ± 0.004	-0.045 ± 0.006
The experiment	0.23 ± 0.08	-0.031 ± 0.008

tant for such an analysis to be repeated now that we are able to provide reliable and consistent experimental values of the total cross sections within 30 MeV of threshold. This is clearly needed to take account of the contributions of the $I=1$ component.

Our value for $|\mathcal{A}_{10}|$ is in good agreement with the value of $8.0\pm0.3m_\pi^{-3}$ obtained by Bernard *et al.* [11] from an analysis of the $\pi^- p\rightarrow\pi^0\pi^0 n$ data of Lowe *et al.* [27]. Table VIII compares our values of the scattering lengths with those of recent theoretical predictions.

Since the value of the scattering lengths obtained from our data are model dependent, they therefore provide a test of heavy baryon chiral perturbation theory (HBχPT). Although there is little controversy in the HBχPT treatment of the physical background to OPE the uncertainties in our experimental values of the scattering lengths are dominated by the uncertainties in the theory [11]. In the case of a_2 the HBχPT calculations converge quickly. As it appears that there are no other prospects for determining this isospin combination of the π-π scattering lengths, we encourage the workers in this field to improve the uncertainties in the calculations, especially that of the $\mathcal{A}_{32}$ amplitude.

Although our (larger) π^- channel cross-section values agree with those of the OMICRON Collaboration (as well as with other data sets), our lower cross-section π^+ channel results disagree with OMICRON but agree instead with those of Sevior [4]. These latter cross sections are sufficiently small that backgrounds constitute a serious problem. The π^- channel OMICRON data with which we agree are those in which a double charge exchange (π^+ to π^-) characterises the reaction, a situation for which OMICRON was better able to discriminate against background than for the lower cross-section π^+ channel where no such charge exchange takes place. A major advantage of our experimental technique is its ability to exploit ''2π'' detection for the π^+ channel in order to discriminate against the many sources of back-ground.

ACKNOWLEDGMENTS

We wish to thank Cam Marshall for constructing and operating the cryogenic targets. We also acknowledge TRIUMF for its support and the Natural Science and Engineering Research Council of Canada for providing the funds needed to perform this experiment.

[1] J. Gasser and M. E. Sevior, Proceedings of the Workshop on Chiral Dynamics (1994), p. 107.

[2] L. Rosselet, P. Extermann, J. Fischer, O. Guisan, R. Mermod, R. Sachot, A. M. Diamant-Berger, P. Bloch, G. Bunce, B. Devaux, N. Do-Duc, G. Marel, and R. Turlay, Phys. Rev. D **15**, 574 (1977).

[3] A. V. Kravtsov, E. A. Lobachev, M. M. Makarov, V. I. Medvedev, V. V. Nelyubin, G. Z. Obrant, V. I. Poromov, V. V. Sarantsev, S. G. Sherman, V. M. Sirin, G. L. Sokolov, and L. N. Tkach, Nucl. Phys. **B134**, 413 (1978).

[4] M. E. Sevior, A. Ambardar, J. T. Brack, P. Camerini, F. Duncan, J. Ernst, A. Feltham, N. Grion, R. R. Johnson, G. Koch, O. Meirav, D. F. Ottewell, R. Rui, G. R. Smith, V. Sossi, D. Theis, and D. Vetterli, Phys. Rev. Lett. **66**, 2569 (1991); Phys. Rev. D **48**, 3987 (1993).

[5] G. Kernel, D. Korbar, P. Križan, M. Mikuž, U. Seljak, F. Sever, A. Stanovnik, M. Starič, D. Zavrtanik, C. W. E. van Eijk, R. W. Hollander, W. Lourens, E. G. Michaelis, N. W. Tanner, S. A. Clark, J. V. Jovanovich, J. D. Davies, J. Lowe, and S. M. Playfer, Z. Phys. C **48**, 201 (1990); G. Kernel *et al.*, Phys. Lett. B **225**, 198 (1989).

[6] C. W. Bjork, S. E. Jones, T. R. King, D. M. Manley, A. T. Oyer, G. A. Rebka, Jr., J. B. Walter, R. Carawon, P. A. M. Gram, F. T. Shively, C. A. Bordner, and E. L. Lomon, Phys. Rev. Lett. **44**, 62 (1980).

[7] H. Burkhardt and J. Lowe, Phys. Rev. Lett. **67**, 2622 (1991); πN Newsletter **6**, 121 (1992)

[8] M. G. Olsson, E. T. Osypowski, and L. Turner, Phys. Rev. Lett. **38**, 296 (1977).

[9] D. Pocanic, E. Frlez, A. Assamagan, J. Chen, K. Keeter, R. Marshall, R. Mine, L. Smith, G. Dodge, S. Hanna, B. King, and J. Knudson, Phys. Rev. Lett. **72**, 1156 (1994).

[10] M. G. Olsson *et al.*, πN Newsletter **10**, 201 (1995).

[11] V. Bernard, N. Kaiser, and Ulf-G. Meißbner, Int. J. Mod. Phys. E **4**, 193 (1995); Nucl. Phys. **B457**, 147 (1995); Nucl. Phys. **A619**, 261 (1997).

[12] K. J. Raywood, A. R. Ambardar, J. B. Lange, and M. E. Sevior, Nucl. Instrum. Methods Phys. Res. A **365**, 135 (1995).

[13] D. Bryman, J. V. Cresswell, M. LeNoble, and R. Poutissou, IEEE Trans. Nucl. Sci. **NS-38**, 295 (1991).

[14] TRIUMF User's Handbook (1987).

[15] G. R. Smith, D. R. Gill, D. Ottewell, G. D. Wait, P. Walden, R. R. Johnson, R. Olszewski, R. Rui, M. E. Sevior, R. P. Trelle, J. Brack, J. J. Kraushaar, R. A. Ristinen, H. Case, E. L. Mathie, V. Pafilis, R. B. Schubank, N. R. Stevenson, A. Rinat, and Y. Alexander, Phys. Rev. C **38**, 240 (1988).

[16] J. Lange Ph.D. thesis, UBC, 1997.

[17] V. Paticchio, G. D'Erasmo, E. M. Fiore, L. Fiore, N. Grion, G. Guarino, A. Pantaleo, and R. Rui, Nucl. Instrum. Methods Phys. Res. A **305**, 150 (1991), and N. R. Stanton, Ohio State University Report, COO 1545–1592 (1971).

[18] J. Spuller, D. Berghofer, M. D. Hasinoff, R. MacDonald, D. F. Measday, M. Salomon, and T. Suzuki, Phys. Lett. **67B**, 479 (1977).

[19] V. L. Highland, M. Salomon, M. D. Hasinoff, E. Mazzucato, D. F. Measday, J.-M. Poutissou, and T. Suzuki, Nucl. Phys. **A365**, 333 (1981).
[20] D. H. Perkins, *Introduction to High Energy Physics* (Addison-Wesley, Reading, MA, 1982), p. 37.
[21] J. B. Birks, *Scintillation Counters* (Pergamon, New York, 1954), pp. 79, 91.
[22] M. F. Rozen (private communication).
[23] V. Bernard, N. Kaiser, and U.-G. Meißbner, Phys. Lett. B **332**, 415 (1994).
[24] GEANT3 Version 3.15, High energy physics detector description and physical process Monte Carlo simulation program, CERN Applications Software Group (Simulation Section), CERN, Geneva, 1991.
[25] M. M. Pavan, Ph.D. thesis, University of British Columbia, 1995, and M. M. Pavan (private comunication).
[26] M. Kermani *et al.*, Phys. Rev. C **58**, 3419 (1998).
[27] J. Lowe, B. Bassalleck, H. B. Burkhardt, W. J. Fickinger, J. R. Hall, M. D. Hasinoff, D. Horvath, G. Koch, K. D. Larson, P. Miller, A. J. Noble, B. L. Roberts, D. K. Robinson, M. Sakitt, M. E. Sevior, N. W. Tanner, C. E. Waltham, T. M. Warner, and D. M. Wolfe, Phys. Rev. C **44**, 956 (1991).
[28] J. Gasser and H. Leutwyler, Phys. Lett. **125B**, 321 (1983); **125B**, 325 (1983).
[29] J. Bijnens *et al.*, Phys. Lett. B **374**, 210 (1996).
[30] L. Girlanda *et al.*, Phys. Lett. B **409**, 461 (1997).